Lithos 125 (2011) 131–150

Contents lists available at ScienceDirect

Lithos

journal homepage: www.elsevier.com/locate/lithos

Post-collisional adakite-like magmatism in the Ağvanis Massif and implications for the evolution of the Eocene magmatism in the Eastern Pontides (NE Turkey)

Gültekin Topuz [a,*], Aral I. Okay [a], Rainer Altherr [b], Winfried H. Schwarz [b], Wolfgang Siebel [c], Thomas Zack [d], Muharrem Satır [c], Cüneyt Şen [e]

[a] Istanbul Technical University, Eurasian Institute of Earth Sciences, Ayazağa 80626, Istanbul, Turkey
[b] Institute of Earth Sciences, University of Heidelberg, Im Neuenheimer Feld 234–236, 69120 Heidelberg, Germany
[c] Institute of Geosciences, University of Tübingen, Wilhelmstr. 56, 72074 Tübingen, Germany
[d] Institute of Geosciences, University of Mainz, Johann-Joachim-Becher Weg 21, 55099 Mainz, Germany
[e] Black Sea Technical University, Department of Geology, 61080 Trabzon, Turkey

ARTICLE INFO

Article history:
Received 27 July 2010
Accepted 13 February 2011
Available online 19 February 2011

Keywords:
Adakite
Post-collisional
Extensional collapse
Ağvanis (Gölova)
Eastern Pontides
NE Turkey

ABSTRACT

In the Anatolia, the Caucasus and northwest Iran, the Eocene epoch is characterized by widespread basic to acidic magmatism, whose temporal and spatial evolutions and origin are poorly understood. In this paper, we provide geochronological and geochemical data on a suite of Early Eocene intrusions from northeast Turkey and discuss their origin within a regional tectonic framework. Post to late-collisional, moderate to small bodies of quartz diorite and leucogranodiorite as well as later dacite porphyries intrude Permo-Triassic low-grade metamorphic rocks in the southern part of the Eastern Pontides very close to the Neo-Tethyan İzmir–Ankara–Erzincan suture. In places, the intrusives display well-developed subsolidus foliations, indicating ongoing penetrative deformation during and shortly after emplacement. Different emplacement depths were inferred based on the contact metamorphic mineral assemblages, Al-in-hornblende barometry and igneous textures (quartz diorite ~14–16 km vs dacitic porphyries ≤7 km). Biotite and hornblende Ar–Ar and zircon U–Pb data indicate that the compositionally and texturally different intrusives were emplaced at ~51 Ma (Ypresian). Three lines of evidence indicate that the Early Eocene represents a tectonically active time with high exhumation rates (≥ 0.6 cm a^{-1}): (i) the quartz diorite and dacitic porphyries were emplaced at different crustal depths, (ii) the emplacement ages of these texturally distinct intrusive rocks are geochronologically undistinguishable, and (iii) intrusive rocks locally show a well-developed foliation. The intrusive rocks display high abundances of Al_2O_3, Sr, Ba, LREEs and low abundances of Y, Sc and HREEs, and are similar to high-silica adakites from supra-subduction zone settings. The geochemical features imply a residual and/or fractionating assemblage rich in hornblende, garnet, pyroxene, and poor in plagioclase. All rock types display similar Sr–Nd isotopic characteristics with initial ε_{Nd} and $^{87}Sr/^{86}Sr$ values ranging from 1.0 to −1.1 and from 0.70421 to 0.70494, respectively. These three coeval rock groups (quartz diorite, leucogranodiorite and dacite porphyries) were generated from a similar source by variable degrees of partial melting and fractionation. These data together with those from the literature clearly reveal that the adakitic signature is common in Paleocene to Early Eocene igneous rocks in northern Turkey on both sides of the İzmir–Ankara–Erzincan suture, but disappears towards the Middle Eocene. Regional geological constraints indicate that the continental collision between the Pontides and the Anatolide–Tauride block occurred in the Paleocene and that the Middle Eocene represents a period of major extension, characterized by a marine transgression. We therefore suggest that the Early Eocene adakitic magmatism in northern Turkey resulted from the presence of a thickened continental crust following the continental collision along the Neo-Tethyan İzmir–Ankara–Erzincan suture whereas the voluminous Middle Eocene magmatism was related to extensional collapse of a thickened orogen.

1. Introduction

Eocene volcano-sedimentary and intrusive rocks cover extensive areas in Turkey (e.g. Keskin et al., 2008; Kürkçüoğlu et al., 2008; Özkaya, 1991; Robertson et al., 2006; Temizel and Arslan, 2009; Yiğitbaş and Yılmaz, 1996), in the Caucasus (e.g. Adamia et al., 1977; Bazhenov and Burtman, 2002; Dilek et al., 2010; Vincent et al., 2005; Yılmaz et al., 2000) and in Iran (e.g. Ramezani and Tucker, 2003; Stöcklin, 1971) (Fig. 1). In Turkey, such rocks occur on both sides of the İzmir–Ankara–Erzincan suture (IAES), which form the tectonic divide between the Pontides and the Anatolide–Tauride

* Corresponding author.
E-mail address: topuzg@itu.edu.tr (G. Topuz).

0024-4937/$ – see front matter © 2011 Elsevier B.V. All rights reserved.
doi:10.1016/j.lithos.2011.02.003

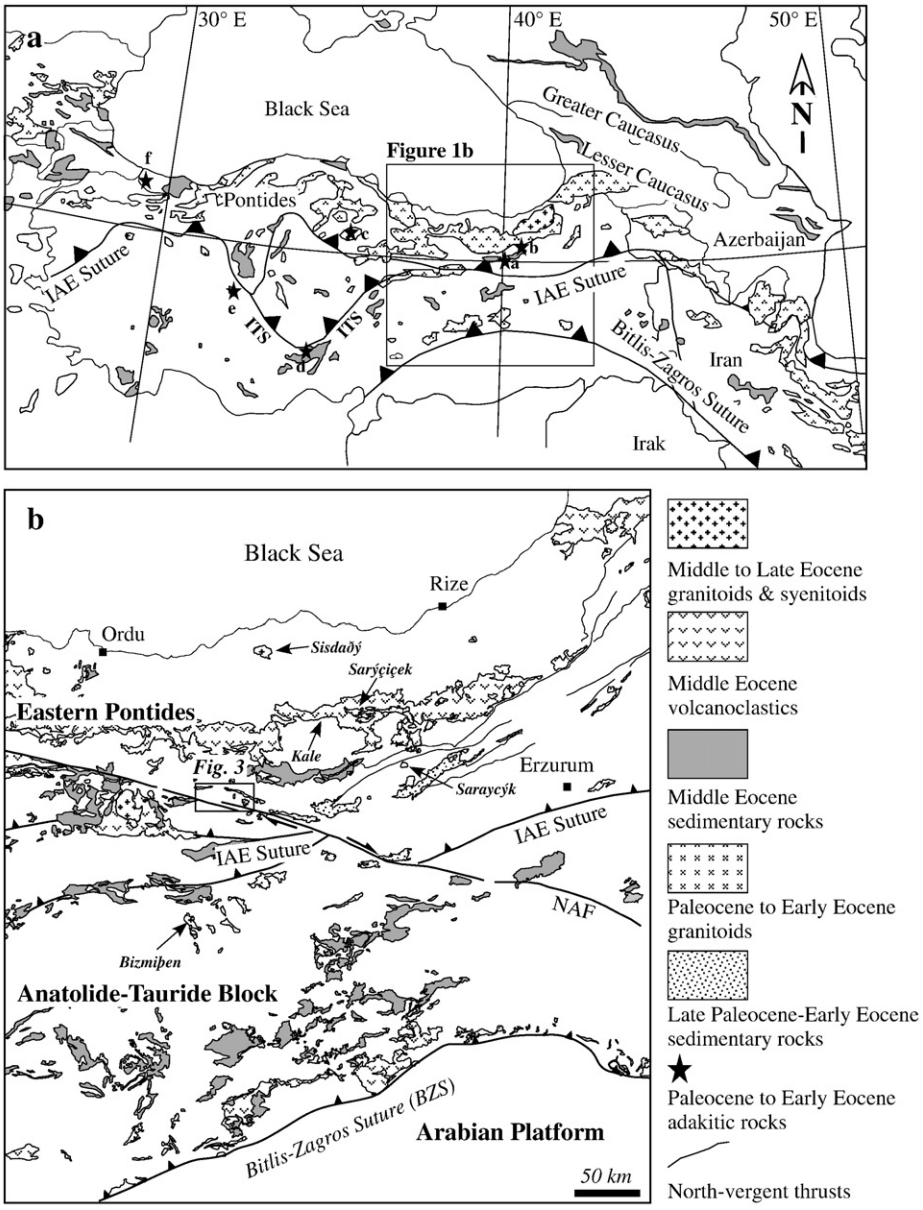

Fig. 1. (a) Distribution of Eocene magmatism in the Anatolia, the Caucasus and northwest Iran together with the main Neo-Tethyan sutures (modified after Vincent et al., 2005). Asterisk stand for localities of Paleocene to Early Eocene adakitic igneous rocks. a Saraycık granodiorite, b Kale volcanics, c Suluova dacites, d Horoz granitoid, e Sivrihisar granodiorite, f Çavuşbaşı granodiorite. (b) Distribution of the Eocene igneous and sedimentary rocks across the transect shown in Fig. 1a.

Block. The southernmost boundary of Eocene igneous and volcano-sedimentary rocks is represented by the Bitlis–Zagros suture (BZS). Such a distribution implies that Eocene magmatism in northern Turkey is post-collisional with respect to the IAES, and was not caused by northward subduction along the IAES, as formerly suggested by Tokel (1977) and Akın (1979). Some recent models proposed for the widespread Eocene magmatism include (i) post-collisional slab-breakoff beneath IAES (Altunkaynak, 2007; Boztuğ et al., 2007; Dilek et al., 2010; Keskin et al., 2008), (ii) back-arc extensional/transtensional events related to northward subduction along the Bitlis–Zagros suture (Robertson et al., 2006, 2007; Vincent et al., 2005), and (iii) post-collisional crustal thickening (Topuz et al., 2005) and delamination of the thickened crust along the IAES (e.g. Dilek et al., 2010; Karslı et al., 2010).

In this paper, we report geological, geochemical and geochronological data on the Early Eocene intrusive rocks from the Ağvanis Massif, Eastern Pontides. The objective is to constrain the causes of the widespread Eocene magmatism in the Eastern Pontides. Our results together with literature data suggest that the Paleocene to Early Eocene magmatism in the whole Pontides displays a pronounced 'adakite-like' signature probably due to the presence of a thickened crust produced by continental collision along the IAES. The 'adakite-like' signature disappears towards the Middle Eocene, suggesting a decrease in crustal thickness due to regional extension.

2. Geological framework

In Turkey, the IAES and BZS represent traces of Neo-Tethyan oceans (Fig. 1a). The İzmir–Ankara–Erzincan ocean between the Anatolide–Tauride block and the Pontides was subducted northward during the Cretaceous giving rise to the submarine magmatic arc of the Eastern Pontides (e.g. Akın, 1979; Okay and Şahintürk, 1997; Okay and Tüysüz, 1999; Şengör and Yılmaz, 1981). The continental collision between the Pontides and the southern Anatolide–Tauride block occurred during the late Paleocene to early Eocene. This is deduced from (i) the north-vergent Paleocene fold-and-thrust belt of the

southern Pontides (Fig. 1b), (ii) the development of Upper Paleocene to Lower Eocene foreland flysch sequences in the southern Pontides and northernmost part of the Anatolide–Tauride block, (iii) post-tectonic, largely undeformed Middle Eocene volcano-sedimentary sequences, which lie unconformably over the north-vergent thrust slices and the IAES, (iv) thermochronological data, which indicate rapid uplift of the Pontides during the Paleocene and Early Eocene (Altherr et al., 2008; Boztuğ et al., 2004; Okay and Şahintürk, 1997; Okay and Tüysüz, 1999). The Intra-Tauride suture (ITS) marks the former existence of another small oceanic basin, generally regarded as a branch of the İzmir–Ankara–Erzincan ocean. Its closure is also estimated to have occured during the Paleocene, based on the age of blueschist-facies metamorphism (Okay and Tüysüz, 1999; Pourteau et al., 2010). The Bitlis–Zagros Neotethyan ocean between the Arabian Platform and the Anatolide–Tauride Block was subducted northward from Late Cretaceous to Oligocene, and final collision occurred by the Miocene (e.g. Şengör and Yılmaz, 1981; Okay et al., 2010, and references therein). This suggests that the İzmir–Ankara–Erzincan and the Intra-Tauride Neotethyan oceans were already closed in the Eocene, while the Bitlis–Zagros Neotethyan ocean was still subducting northwards.

The Eocene rocks in the Eastern Pontides lie with a major angular unconformity over all the older units, ranging in age from Early Carboniferous to Early Paleocene. This implies major uplift and erosion during the Paleocene. The Eocene rocks in the Eastern Pontides consist of a Late Paleocene-Early Eocene flyschoid sequence (e.g. Okay et al., 1997; Rice et al., 2009) and a Middle Eocene (Lutetian) volcano-sedimentary sequence (Figs. 1b and 2) (Aslan, 2010; Kaygusuz et al., 2011; Temizel and Arslan, 2009; Tokel, 1977). Both sequences are not in mutual contact, suggesting a time gap between their depositions. The Paleocene to Early Eocene flyschoid sequence consists of conglomerate (several hundred meters thick) at the base passing into a sandstone-shale turbidite sequence (over 1000 m thick), and were interpreted as foreland basin developed in front of the northward advancing thrust sheet (Okay and Şahintürk, 1997; Okay et al., 1997). The Middle Eocene (Lutetian) volcano-sedimentary sequence is exposed over large areas, locally sealing the boundary between the Eastern Pontides and the Anatolide–Tauride block (Fig. 1b). Volcanic members of this sequence include basaltic to dacitic pyroclastics and rare flows with calc-alkaline affinity (e.g. Aslan, 2010; Kaygusuz et al., 2011; Temizel and Arslan, 2009). The Middle Eocene volcano-sedimentary rocks represent a major marine transgression and were deposited in a shallow-marine environment during an extensional tectonic regime (Okay and Şahintürk, 1997). The Middle Eocene extensional regime was of relatively short duration, and the Eastern Pontides was uplifted above sea level during the Oligocene, as revealed by the absence of Oligocene marine sedimentary rocks. In clear distinction to the sedimentary successions, ages of the dated igneous rocks in the Eastern Pontides span the whole Paleocene and Eocene time with no obvious gap (Fig. 2, e.g. Aslan, 2010; Boztuğ, 2008; Boztuğ et al., 2006, 2007; Karslı et al., 2007, 2010; Kaygusuz et al., 2011; Topuz et al., 2005). However, Paleocene to Early Eocene igneous rocks are much less voluminous than the Middle Eocene ones (Fig. 1b).

In the Anatolide–Tauride block, the Eocene volcanoclastic and intrusive rocks are concentrated close to the BZS or the IAES (Elmas and Yılmaz, 2003; Karaoğlan et al., 2009; Kuşçu et al., 2010; Önal et al., 2005; Rice et al., 2009; Robertson et al., 2006, 2007; Yiğitbaş and Yılmaz, 1996) (Fig. 1b). In the central parts of this block, sedimentary rocks predominate. Similar to the Eastern Pontides, the Eocene sedimentary rocks are represented by two sequences (Gürbüz and Gül, 2005; Türkmen et al., 2001): (i) Late Paleocene to Early Eocene limestones, siltstones and mudstones and (ii) Middle Eocene to Oligocene conglomerates, sandstones, limestones and marls. The Late Cretaceous to Middle Eocene igneous rocks in the southern part of the Anatolide–Tauride block were ascribed to the subduction along the Bitlis–Zagros suture (e.g. Karaoğlan et al., 2009). In contrast to the Eastern Pontides and the Anatolide–Tauride block, the Early to Late Eocene rocks on the Arabian platform consist of sedimentary rocks without any volcanic input (Perinçek, 1990).

3. Local geology and field relations

The Ağvanis Massif is a fault-bounded block of metamorphic rocks, ~20 km long and ~6 km wide, which are intruded by Eocene magmatic rocks (Fig. 3). The metamorphic rocks include metabasites, phyllites and marbles, metamorphosed at greenschist- to albite-epidote amphibolite-facies conditions (Nebert, 1961; Okay, 1984). The age of metamorphism is older than 209 ± 1 Ma (Late Triassic or earlier), as indicated by disturbed incremental Ar–Ar age spectra of white micas (Topuz et al., in prep.). The metamorphic rocks are pierced by a number of Eocene intrusions, comprising quartz diorite and leucogranodiorite, as well as numerous younger dacite porphyry dikes. These intrusives, the topic of this paper, display locally well-developed foliations, and hence some of them were erroneously

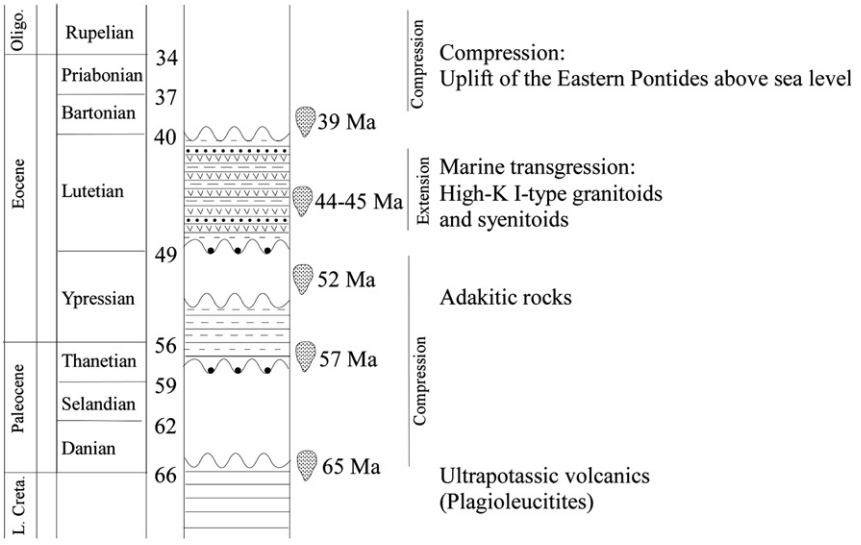

Fig. 2. Regional stratigraphy and ages of the granitoid intrusions. Geological time scale is from Gradstein et al. (2004). Tha data are compiled from Okay and Şahintürk (1997), Topuz et al. (2005), Boztuğ et al. (2006, 2007), Boztuğ (2008), Altherr et al. (2008) and Karslı et al. (2007, 2010).

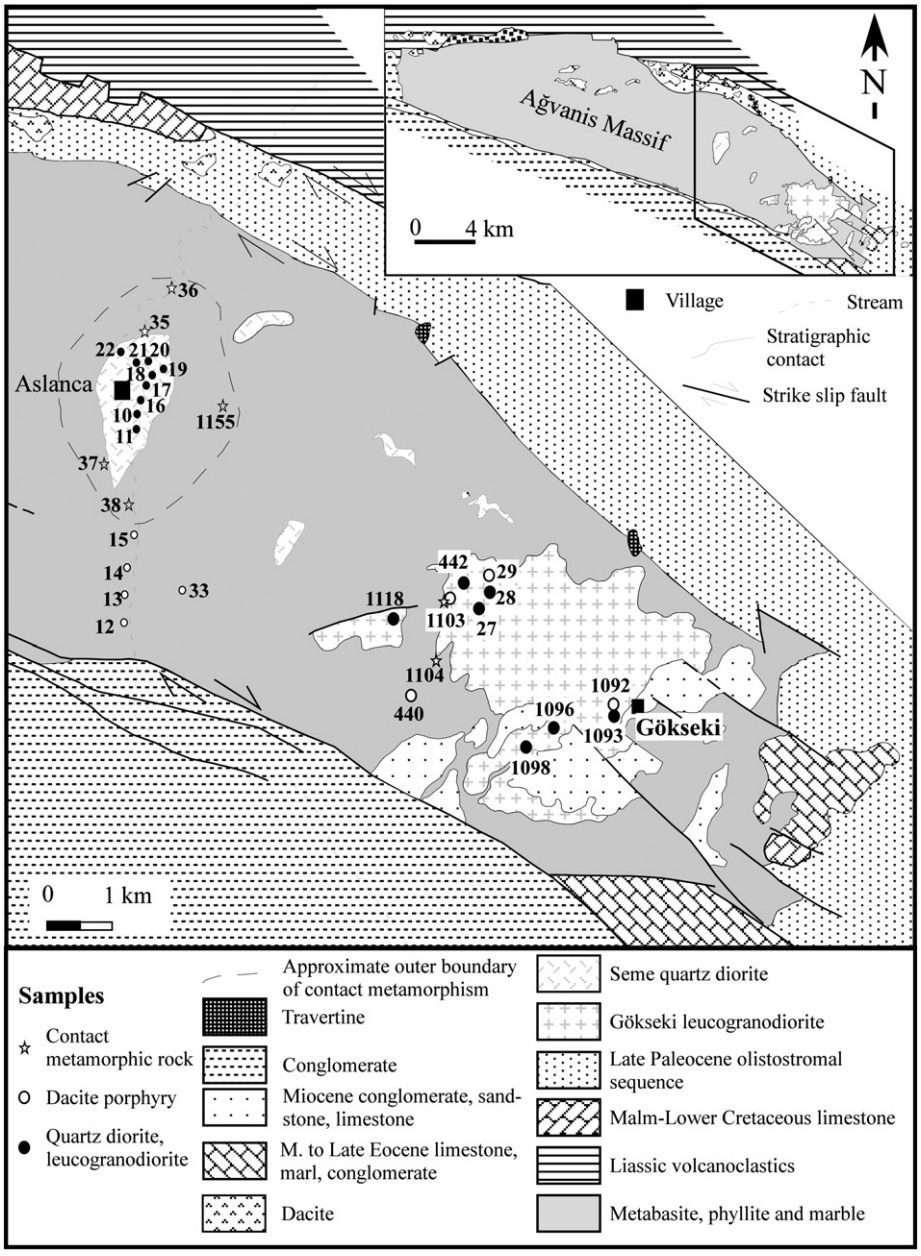

Fig. 3. Geological map of the Seme quartz diorite and the Gökseki leucogranodiorite together with the sample locations (see inset for location). Inset shows the geological map of the Ağvanis Massif (modified after Okay, 1984).

regarded as premetamorphic in earlier studies (e.g. Altınkaynak, 2001; Nebert, 1961; Okay, 1984).

The Seme quartz diorite forms several small intrusions within the metamorphic rocks (Okay, 1984) (Fig. 3). Mafic microgranular enclaves (up to 0.8 m in diameter) are common. Contacts between these enclaves and the host quartz diorite are sharp to gradual, implying that both magmas crystallized concurrently. Around the intrusion, a contact metamorphic aureole (~1.5 km wide) is developed in the regional-metamorphic phyllites and metabasites (Okay, 1984; own observations). The quartz diorite and its metamorphic country rocks contain numerous dikes of dacite porphyry (<10 m thick) and aplite (<40 cm thick), some of which display a weak foliation.

At the eastern end of the Ağvanis Massif, the Gökseki leucogranodiorite crops out in an area of ~10 km^2 (Fig. 3). Locally, this medium-grained intrusive rock is foliated. In marginal domains of this intrusion, exogenic enclaves from the country rocks (up to 2 m in diameter) are common. Their foliations are oriented accidentally and are not parallel to the local foliation of the leucogranodiorite, which is cut by dikes of dacite porphyry and leucogranite (<3 m thick). Contact metamorphic effects are observed, but not as clearly as around the Seme quartz diorite.

In addition to the intrusive rocks in the Ağvanis Massif, highly altered white dacitic rocks of Early Eocene age occur in the Paleocene olistromal sequence (Fig. 3). These dacites are outside the scope of the paper.

4. Analytical techniques

Mineral analyses were carried out at the Institute of Earth Sciences at Heidelberg with a CAMECA SX51 electron microprobe equipped with five wavelength-dispersive spectrometers. Standard operating conditions were 15 kV accelerating voltage, 20 nA beam current and a beam diameter of ~1 μm. Counting times were usually 10 s except for Mg, Ca and Al (20 s), and Ti (30 s) in oxides. Feldspars were analysed with a defocused beam (10 μm) in order to minimize loss of alkalis. Natural and synthetic oxide and silicate standards were used for

calibration. The PAP algorithm (Pouchou and Pichoir, 1984, 1985) was applied to raw data.

Whole-rock analyses were performed at Acme Analytical Laboratories Ltd. in Vancouver (Canada) by ICP emission spectrography (Jarrel Ash AtomComb 975) for major elements and the trace elements Ba, Nb, Ni, Sr, Sc, Y and Zr, and an ICP mass spectrometer (Perkin-Elmer Elan 6000) for the determination of other trace elements including rare earth elements. Analytical procedures and levels of uncertainty are the same as outlined in Topuz et al. (2010).

Sr and Nd isotope analyses were performed at the Institute of Geosciences, Tübingen, by thermal ionization mass spectrometry using a Finnigan MAT 262 mass spectrometer. Rock powders were dissolved in 52% HF for four days at 140 °C on a hot plate. Digested samples were dried and redissolved in 6 N HCl, dried again and redissolved in 2.5 N HCl. Sr and light rare earth elements were isolated on quartz columns by conventional ion exchange chromatography with a 5 ml resin bed of Bio Rad AG 50 W-X12, 200–400 mesh. Nd was separated from other rare-earth elements on quartz columns using 1.7 ml Teflon powder coated with HDEHP, di(2-ethylhexyl)orthophosphoric acid, as cation exchange medium. Sr was loaded with a Ta–HF activator on pre-conditioned W filaments and was measured in single-filament mode. Nd was loaded as phosphate on pre-conditioned Re filaments and measurements were performed in a Re double filament configuration. The $^{87}Sr/^{86}Sr$ isotope ratios were normalized to $^{86}Sr/^{88}Sr = 0.1194$ and the $^{143}Nd/^{144}Nd$ isotope ratios to $^{146}Nd/^{144}Nd = 0.7219$. The La Jolla Nd standard yielded $^{143}Nd/^{144}Nd$ value of 0.511842 ± 0.000008 (reference value 0.511850) and the NBS 987 Sr standard yielded $^{87}Sr/^{86}Sr$ value of 0.710257 ± 0.000008 (reference value 0.710248). Total procedural blanks (chemistry and loading) were 134 pg for Nd and 333 pg for Sr.

$^{40}Ar/^{39}Ar$ dating was carried out at the Institute of Earth Sciences at Heidelberg by a MAT GD-150 gas mass spectrometer (0.38 T permanent magnet, 180°, 5 cm radius of curvature). Measured argon contents were corrected for mass discrimination, isotopic interferences, furnace and line blanks. Ages were calculated against the BMus/2 flux monitor ($t = 328.5 \pm 1.1$ Ma (Schwarz and Trieloff, 2007) using the decay constants recommended by Steiger and Jäger (1977)).

LA–ICP–MS analyses for the zircons were performed at the Institute of Geosciences at Mainz, utilizing a system consisting of a New Wave 213 nm laser coupled to an Agilent 7500ce quadrupole ICP–MS. Analytical procedures are the same as outlined in Topuz et al. (2010).

5. Petrography and mineral compositions

The Seme quartz diorite (I-type) is medium-grained and consists of plagioclase, hornblende, biotite, quartz, K-feldspar, epidote, titanite and clinopyroxene accompanied by accessory titanomagnetite, apatite and zircon (Fig. 4a and b). Plagioclase (An_{41-16}) forms early euhedral grains with normal zoning. Hornblende is hypidiomorphic and contains inclusions of biotite, apatite, titanomagnetite, quartz and rare resorbed clinopyroxene. The composition of hornblende is characterized by 7.3–9.4 wt.% Al_2O_3, 0.58–1.67 wt.% TiO_2, 0.6–1.0 wt.% K_2O and X_{Mg} [$= Mg/(Mg + Fe_{tot})$] = 0.63–0.70 (Table 1). Clinopyroxene has X_{Mg} values of ~0.74 and Al_2O_3 contents between 1 and 2 wt.%. Biotite contains large numbers of apatite inclusions and shows X_{Mg} values of 0.55–0.61 and low Ti contents of 0.09–0.18 cations pro formula unit (cpfu) (Table 1). Locally, symplectitic intergrowths of biotite and quartz are found. Abundant euhedral titanite may contain resorbed inclusions of Fe–Ti oxides (Fig. 4a). Quarz and K-feldspar (Or_{88-95}) are minor constituents and are confined to the interstices. Myrmekitic intergrowth of plagioclase and quartz is common. Hypidiomorphic to xenomorphic epidote occurs as inclusion in hornblende, biotite and plagioclase (Fig. 4b) and is relatively rich in iron [$Fe^3+/(Fe^3+ + Al) = 0.29–0.31$], corresponding to pistacite$_{87-93}$. Besides primary epidote, there is some secondary epidote occurring together with calcite along cracks in plagioclase.

Mafic microgranular enclaves in the Seme quartz diorite consist of the same minerals as the host rock. Biotite, hornblende and clinopyroxene are compositionally similar to those in the host quartz diorite (Table 1). Plagioclase, on the other hand, is somewhat richer in anorthite (An_{61-23}). Titanite occurs as primary euhedral grains with magnetite inclusions and as small, secondary xenomorphic grains around biotite. Minor amounts of small K-feldspar grains fill the interstitial spaces.

Aplitic dikes consist of plagioclase (An_{24-01}), K-feldspar (Or_{86-99}), quartz, minor chloritized biotite, and accessory titanite, apatite and zircon. Locally, quartz and K-feldspar form micrographic intergrowths.

The Gökseki leucogranodiorite consists of plagioclase, quartz, biotite and minor interstitial K-feldspar. Accessory phases include apatite, allanite, zircon and magnetite. Locally, the leucogranodiorite is hydrothermally altered and secondary minerals such as calcite, chlorite, sericite, hematite and anatase have formed. In places, the intrusive body displays a well-developed foliation. While plagioclase and minor alkali feldspar are either undeformed or show brittle deformation, quartz is dynamically recrystallized and wraps passively around feldspar aggregates. Biotite may show fish-shaped boudinaged grains (Fig. 4c and d). These textural features suggest deformation under low-grade conditions (~250–300 °C; Passchier and Trouw, 2005). Plagioclase forms relatively euhedral grains with compositional zoning (An_{39-19}), while minor K-feldspar (Or_{87-96} Ab_{13-04}) occurs as interstitial grains in less deformed domains, locally incorporating grains of euhedral plagioclase and quartz. Biotite is locally bent and has X_{Mg} values of 0.46–0.55 and Ti contents of 0.17–0.26 cpfu (Table 1). Minerals in the leucogranitic dikes display more evolved compositions (plagioclase An_{28-14}; biotite $X_{Mg} = 0.32–0.35$).

Dacite porphyries are characterized by a porphyric texture (Fig. 4e and f) with phenocrysts of plagioclase, hornblende and biotite and minor amounts of quartz. In addition, these rocks may contain alkali feldspar, titanite, magnetite, apatite and zircon. Some of the porphyries display a foliation defined by a parallel alignment of hornblende and biotite (Fig. 4e), indicating emplacement under differential stress. Some of the dacitic dikes are hydrothermally altered and contain abundant muscovite, epidote and calcite. Plagioclase phenocrysts display normal zoning (An_{55-25}) and have higher anorthite contents than matrix plagioclase (An_{28-14}). Hornblende may show chemical zonation and is characterized by relatively high contents of Al_2O_3 (15.3–10.9 wt.%) (Table 1). Biotite shows X_{Mg} values between 0.46 and 0.58 and Ti contents of 0.103–0.209 cpfu. Alkali feldspar ($X_{Or} = 0.89–0.96$) is intergrown with quartz and is confined to the groundmass.

6. Bulk-rock chemistry

The intrusive rocks span a wide range of compositions (Table 2, Fig. 5). The aluminum saturation index [ASI = molar $Al_2O_3/(CaO + K_2O + Na_2O)$] increases with SiO_2 from 0.64 to 1.11 (Fig. 7a). The rocks belong to the medium-K series as defined by Peccerillo and Taylor (1976). With increasing SiO_2, the abundances of TiO_2, $Fe_2O_3^{tot}$, MgO, CaO, P_2O_5, Sc, V, Co, Ni, Cr, Zn, REE, Nb, Ta and Y decrease (Fig. 5, not all elements are shown). Mafic microgranular enclaves of the Seme quartz diorite are characterized by relatively low contents of Al_2O_3, Sr, Ba, Zr and Hf. The other samples show negative correlations between most of these elements and SiO_2, while K_2O, Na_2O, Rb and Pb are nearly constant (except for the leucogranitic and aplitic dikes).

Samples from the Seme quartz diorite form three compositional groups: a more mafic type with $SiO_2 \approx 58.5$ wt.%, a normal type with $SiO_2 \approx 62.1–64.5$ wt.%, and mafic microgranular enclaves that show dioritic compositions with $SiO_2 \approx 50.9–54.8$ wt.%. The Gökseki leucogranodiorite and its leucogranitic dikes, together with aplitic dikes from the Seme quartz diorite intrusion plot at the high-SiO_2 end of the trends. The younger dacite porphyries form a nearly coherent range of

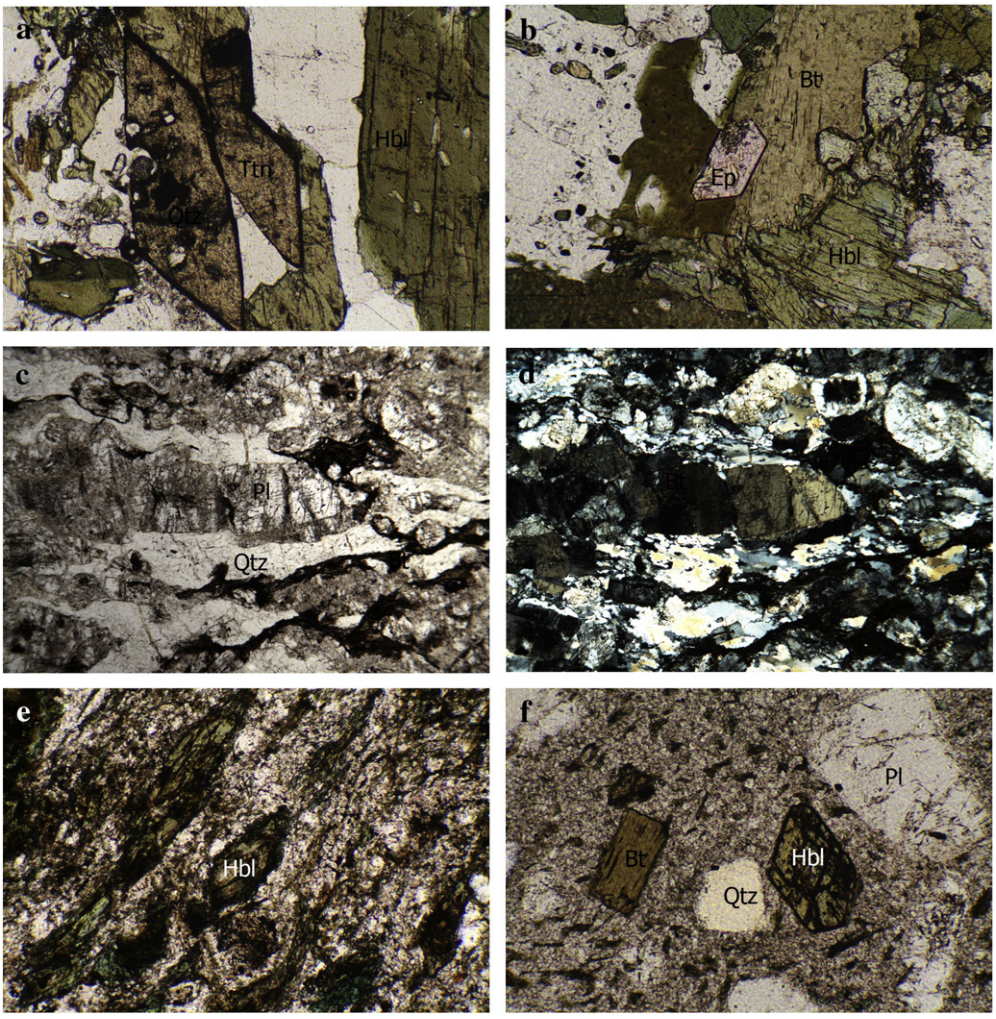

Fig. 4. Micrographs illustrating the microtextural features of the Gökseki leucogranodiorite, Seme quartz diorite and dacitic porphyries. (a) Idiomorphic titanite grains with Fe–Ti oxide inclusions in the Seme quartz diorite (sample 22A). (b) A relatively idiomorphic epidote grain in the biotite grain (sample 18A). (c–d) A foliated leucogranodiorite with dynamically recrystallized quartz grains and plagioclase porphyroclasts. Note that the foliation is defined by recrystallized quartz and biotite (sample 1093). (e) A well-foliated dacite porphyry in which the foliation is defined by hornblende and recrystallized biotite (sample 440). (f) Unfoliated dacitic porphyry with phenocrysts of hornblende, plagioclase and minor biotite (sample 13). In all micrographs, the width corresponds to 1.5 mm.

compositions, bridging the gap between the samples from the Seme quartz diorite and those from the Gökseki leucogranodiorite (Fig. 5).

On primitive mantle-normalized element concentration diagrams (Fig. 6) all samples from the Seme quartz diorite display negative anomalies in Rb–Ba, Nb–Ta, P and Ti, but positive anomalies in Sr. The mafic microgranular enclaves, on the other hand, have pronounced negative anomalies in Ba, Nb–Ta and Zr–Hf. The Gökseki leucogranodiorite and the dacite porphyries show similar features with negative anomalies in Nb–Ta, P and Ti, and positive anomalies in K, Pb and Sr. In the hydrothermally overprinted samples (13, 1118 and 1124), the positive Pb anomaly disappears or a negative Pb results. Chemical variations among the dacite porphyries do not depend on the type of country rock (i.e. Seme quartz diorite, Gökseki leucogranodiorite or metamorphic rocks).

Chondrite-normalized (cn) rare earth element (REE) patterns (Fig. 7) of the Seme quartz diorite, the Gökseki leucogranodiorite and the dacite porphyries are generally characterized by high $(La/Yb)_{cn}$ ratios (13.3–46.3) and by the absence of significant negative Eu anomalies, with $Eu/Eu^* [= Eu_{cn}/(Sm_{cn} \cdot Gd_{cn})^{0.5}]$ ranging from 0.91 to 1.17 (Table 2). In addition, the HREE patterns (from Er to Lu) are hardly fractionated. The aplite in the Seme quartz diorite shows a similar REE pattern, but has a higher positive Eu anomaly ($Eu/Eu^* = 1.29$), while the leucogranitic dike in the Gökseki leucogranodiorite has a U-shaped pattern with $(La/Yb)_{cn} = 8.3$ (not shown, Table 2). The mafic enclaves of the Seme quartz diorite are characterized by moderate negative Eu anomalies and LREE convex-upward shapes.

The Seme quartz diorite has high Mg# [$= 100 * MgO/(MgO + FeO_{tot})$] values (55.7–57.7), but low Ni contents (9.2–15.3 ppm; Table 2). Mg# values and Ni contents of the mafic microgranular enclaves are slightly higher (57.6–60.7 and 12.2–29.4 ppm, respectively). The aplitic dike shows a significantly lower Mg# value of 31.6. The Gökseki leucogranodiorite has low Mg# values of ~37, but the Mg# values of the dacite porphyries range from 43.2 to 62.7.

Compositionally, all rock types (except for the Seme aplite and the Gökseki leucogranite), show a distinct 'adakitic flavor', with many geochemical signatures being similar to those of HSA (= high-silica adakites) (Martin et al., 2005; Moyen, 2009), such as (i) low K_2O/Na_2O ratios (0.33–0.70) and relatively high MgO and Al_2O_3 contents; (ii) low contents of garnet-compatible trace elements (Y, HREE, Sc), (iii) high ratios of chondrite normalized La/Yb (13.3–46.3) and Sr/Y (60–180) (Fig. 8), (iv) high abundances of plagioclase-compatible Sr (574–1270 ppm), and (v) absence of significant Eu anomalies (Fig. 7).

7. Radiometric dating

Zircon grains from the Gökseki leucogranodiorite are prismatic with aspect ratios of 2 to 3 and display oscillatory zoning (Fig. 9). Inclusions of quartz, biotite and plagioclase are common. 14 zircon grains from

Table 1
Selected microprobe analyses of hornblende and biotite from the intrusive rocks in the Ağvanis Massif. NE Turkey.

Sample	11a	11a	18A	22A	18A	22B	11B	11B	23E	440	11A	18A	22A	18A	22B	1093	27	11B	23e	1092
Rock type	QD	QD	QD	QD	ME	ME	DP	DP	DP	DP	QD	QD	QD	ME	ME	LGR	LG	DP	DP	DP
SiO_2	46.52	44.96	45.21	45.94	45.7	45.61	43.01	41.68	41.00	38.89	37.73	37.52	37.84	37.53	37.70	35.81	35.83	37.74	35.76	36.69
TiO_2	1.25	0.58	1.33	1.52	1.17	1.22	1.83	1.97	1.93	2.21	1.77	2.92	2.58	1.70	2.14	3.66	1.85	2.63	3.24	3.65
Al_2O_3	7.33	9.10	7.61	8.30	8.03	8.41	11.93	13.79	15.26	14.93	15.21	14.51	14.89	14.8	14.64	15.02	17.48	14.66	15.43	14.69
Cr_2O_3	0.04	0.02	0.02	0.03	0.04	0.01	0.00	0.01	0.00	0.05	0.00	0.04	0.00	0.06	0.00	0.04	0.02	0.00	0.06	0.02
FeO_{tot}	13.84	15.8	15.03	15.13	14.04	15.72	14.01	14.81	10.07	13.81	16.58	16.91	16.75	15.94	17.08	20.62	22.18	17.44	18.39	17.95
MnO	0.35	0.31	0.43	0.36	0.43	0.29	0.24	0.17	0.06	0.21	0.25	0.19	0.30	0.26	0.26	0.43	0.91	0.22	0.27	0.36
MgO	13.01	11.67	12.53	12.03	12.90	11.96	12.07	10.9	13.58	11.89	13.69	13.45	13.08	15.07	13.38	10.04	6.70	12.43	11.94	12.22
CaO	11.72	11.59	11.69	11.88	11.78	11.75	11.04	10.9	11.52	11.48	0.08	0.18	0.00	0.19	0.05	0.06	0.08	0.00	0.00	0.04
Na_2O	1.23	1.27	1.49	1.32	1.12	1.24	1.92	1.98	2.39	2.42	0.08	0.06	0.07	0.07	0.07	0.09	0.07	0.06	0.05	0.07
K_2O	0.76	0.92	0.92	0.84	0.98	0.94	0.50	0.47	0.95	0.89	9.22	8.88	9.25	8.82	9.09	9.13	9.19	9.19	9.15	9.34
Total	96.04	96.22	96.25	97.36	96.17	97.14	96.55	96.68	96.74	96.78	94.61	94.67	94.76	94.42	94.41	94.89	94.29	94.36	94.30	95.01
Cations on the basis of 23 oxygens and 13 cations excluding Ca, Na and K											Cations on the basis of 11 oxygens									
Si	6.920	6.718	6.771	6.804	6.797	6.763	6.328	6.143	5.979	5.769	2.852	2.838	2.859	2.832	2.863	2.769	2.802	2.872	2.750	2.794
$Al^{(IV)}$	1.080	1.282	1.229	1.196	1.203	1.237	1.672	1.857	2.021	2.231	1.148	1.162	1.141	1.168	1.137	1.231	1.198	1.128	1.250	1.206
$Al^{(VI)}$	0.205	0.320	0.114	0.252	0.204	0.233	0.397	0.539	0.601	0.379	0.207	0.132	0.184	0.149	0.173	0.138	0.413	0.187	0.149	0.113
Ti	0.140	0.065	0.150	0.169	0.131	0.136	0.203	0.218	0.212	0.247	0.101	0.166	0.147	0.096	0.122	0.213	0.109	0.150	0.187	0.209
Cr	0.005	0.002	0.002	0.004	0.005	0.001	0.000	0.001	0.000	0.006	0.000	0.002	0.000	0.003	0.000	0.003	0.001	0.000	0.003	0.001
Fe^{3+}	0.357	0.576	0.454	0.294	0.470	0.463	0.749	0.783	0.546	0.840	0.000	0.000	0.000	0.000	0.000	0.000	0.000	0.000	0.000	0.000
Fe^{2+}	1.365	1.398	1.428	1.579	1.276	1.487	0.975	1.042	0.682	0.873	1.048	1.070	1.058	1.006	1.084	1.333	1.450	1.110	1.183	1.143
Mn	0.044	0.039	0.055	0.045	0.054	0.036	0.030	0.021	0.007	0.026	0.016	0.012	0.019	0.016	0.017	0.028	0.060	0.014	0.018	0.023
Mg	2.885	2.599	2.797	2.656	2.860	2.644	2.647	2.395	2.952	2.629	1.542	1.517	1.473	1.695	1.514	1.157	0.781	1.410	1.369	1.387
Ca	1.868	1.855	1.876	1.885	1.877	1.867	1.740	1.721	1.800	1.824	0.007	0.015	0.000	0.016	0.004	0.005	0.007	0.000	0.000	0.003
Na	0.354	0.368	0.432	0.379	0.323	0.356	0.548	0.566	0.675	0.696	0.011	0.009	0.011	0.010	0.011	0.014	0.010	0.008	0.008	0.010
K	0.144	0.175	0.176	0.159	0.186	0.178	0.094	0.088	0.177	0.168	0.889	0.857	0.892	0.849	0.880	0.901	0.916	0.892	0.898	0.907
X_{Mg}	0.68	0.65	0.66	0.63	0.69	0.64	0.73	0.70	0.81	0.75	0.60	0.59	0.58	0.63	0.58	0.46	0.35	0.56	0.54	0.55

Rock types: QD = Seme quartz diorite; ME = mafic enclave; and DP = dacite porphyre. X_{Mg} is $Mg/(Mg + Fe^{2+})$.

Table 2
Whole-rock analyses of selected samples from the intrusive rocks in the Ağvanis Massif, NE Turkey.

Samples	10A	11A	16A	17A	18A	20A	21A	22A	23A	17D–E	18A–E
Rock type	QD	QD	QD	QD	QD	QD	QD	QD	QD	ME	ME
Setting	Seme	Seme	Seme	Seme	Seme	Seme	Seme	Seme	Seme	Seme	Seme
SiO_2	63.87	58.70	63.37	63.25	64.50	62.01	62.58	61.67	58.63	54.77	52.65
TiO_2	0.53	0.71	0.55	0.51	0.51	0.61	0.58	0.62	0.76	0.88	1.11
Al_2O_3	16.27	17.34	16.18	16.01	16.26	16.95	16.62	16.97	17.01	15.79	15.55
$Fe_2O_3^{tot}$	3.52	5.03	3.81	3.62	3.57	4.07	4.02	4.16	5.18	6.91	8.64
MnO	0.06	0.09	0.07	0.06	0.06	0.07	0.07	0.07	0.09	0.14	0.16
MgO	2.29	3.40	2.47	2.38	2.30	2.70	2.56	2.84	3.45	5.00	6.74
CaO	4.66	6.21	4.87	4.91	4.92	5.48	5.34	5.59	6.55	8.17	7.29
Na_2O	4.56	4.57	4.36	4.36	4.48	4.64	4.61	4.53	4.66	4.64	3.91
K_2O	2.59	1.75	2.65	2.62	2.45	2.15	2.01	2.12	1.92	0.94	2.04
P_2O_5	0.28	0.42	0.30	0.31	0.28	0.34	0.33	0.36	0.46	0.56	0.57
LOI	1.20	1.60	1.20	1.80	0.50	0.80	1.10	0.90	1.10	2.10	1.20
Total	99.84	99.83	99.84	99.84	99.84	99.83	99.83	99.83	99.81	99.92	99.90
Sc	7	11	8	7	8	8	8	9	11	18	22
Ni	10.7	16.5	11.1	10.1	9.2	12.5	13.4	14.1	15.3	12.2	29.4
Co	10.6	15.6	11.8	11.5	10.4	13.7	11.9	13.3	16.2	22.5	30.1
V	81	117	91	83	82	100	95	103	125	184	197
Cu	27.8	25.8	55.3	5.5	12.9	8.0	11.7	4.7	13.4	37.1	6.3
Zn	28	39	27	26	23	21	36	32	32	30	73
Cs	2.9	3.3	3.6	3.9	3.7	2.4	3.1	2.7	6.0	2.0	10.5
Rb	73	56	82	81	71	65	60	60	62	37	123
Ba	739.5	571.5	790.3	746.6	705.6	862.4	714.7	638.6	684.6	169.4	255
U	3.4	2.2	2.8	3	3.8	2.3	2.3	2.4	2.6	0.8	2.4
Th	12.9	12.2	13.1	14.5	16.1	12.0	14.0	12.5	9.4	4.3	6.9
Pb	5.0	4.5	4.0	3.5	3.0	4.5	3.0	3.5	4.0	3.5	3.5
Sr	1056	1160	1048	1014	1060	1195	1142	1224	1270	942	746
Nb	12.2	13.4	11.7	10.4	12.3	11.3	11.6	12.3	15.1	12.7	15.9
Ta	0.7	0.8	0.7	0.5	0.8	0.6	0.6	0.8	0.8	0.6	0.5
Zr	126	149	163	129	124	144	165	120	147	123	156
Hf	3.2	3.5	3.7	3.4	3.5	3.6	3.9	3.1	3.4	2.9	3.9
Y	9.1	12.5	8.6	7.8	9.8	9.4	9.7	11.0	13.1	15.0	13.9
Ga	20.0	21.4	19.1	20.0	19.8	20.8	19.8	19.8	20.9	19.8	22.8
Cr	55	41	41	41	41	41	34	48	48	103	212
La	35.2	50.8	36.3	31.4	29.1	54.3	49.3	41.6	42.3	43.3	34.5
Ce	72.0	97.4	71.7	64.9	65.7	97.8	91.9	82.1	90.5	94.4	78.8
Pr	8.02	10.83	7.95	7.17	7.68	10.27	9.67	9.33	10.59	11.57	9.74
Nd	27.1	37.1	26.7	24.4	25.9	32.3	31.9	32.3	37.7	42.2	36.9
Sm	3.80	5.00	3.60	3.40	3.80	4.30	4.20	4.80	5.40	6.10	5.40
Eu	1.00	1.29	0.99	0.92	1.02	1.09	1.07	1.28	1.42	1.15	1.06
Gd	2.73	3.78	2.62	2.41	2.90	3.00	2.93	3.40	4.00	4.54	4.29
Tb	0.40	0.53	0.35	0.34	0.39	0.41	0.43	0.47	0.55	0.65	0.58
Dy	1.95	2.74	1.78	1.76	1.94	2.00	2.14	2.51	2.83	3.36	2.96
Ho	0.35	0.48	0.32	0.28	0.38	0.35	0.37	0.41	0.49	0.59	0.55
Er	0.80	1.11	0.73	0.76	0.89	0.85	0.83	0.99	1.18	1.30	1.23
Tm	0.11	0.16	0.11	0.11	0.14	0.13	0.14	0.14	0.16	0.19	0.18
Yb	0.79	1.03	0.70	0.70	0.88	0.79	0.82	0.91	1.12	1.29	1.17
Lu	0.11	0.16	0.12	0.11	0.15	0.11	0.12	0.14	0.17	0.19	0.19
K_2O/Na_2O	0.57	0.38	0.61	0.60	0.55	0.46	0.44	0.47	0.41	0.20	0.52
Mg#	56.28	57.22	56.19	56.54	56.04	56.76	55.75	57.46	56.86	58.88	60.68
ASI	0.87	0.84	0.86	0.85	0.86	0.85	0.85	0.85	0.79	0.67	0.71
$(La/Yb)_{cn}$	30.04	33.25	34.96	30.24	22.29	46.34	40.53	30.82	25.46	22.63	19.88
Eu/Eu*	0.95	0.91	0.99	0.98	0.94	0.93	0.93	0.97	0.93	0.67	0.67

Rock types: QD = Seme quartz diorite. ME = mafic enclave; A = aplite; DP = dacitic porphyries; LGR = leucogranodiorite; LG = Leucogranite; Meta. Dike or sills in the metamorphics; Mg# = 100 * (MgO/(MgO + FeO_{tot})) in molar porportions; ASI = aluminum saturation index = molar $Al_2O_3/(CaO + Na_2O + K_2O)$; $(La/Yb)_{cn}$ = chondrite-normalized La/Yb ratio; oxides are given in wt%. trace elements in μg/g.

sample 28 were analysed for their U–Pb isotopic compositions by LA–ICP–MS, yielding a weighted mean age of 51.1 ± 1.0 Ma (2σ, Fig. 10). High U contents (305–1034 ppm) and relatively high Th/U ratios (0.38 to 1.04) are characteristic of magmatic zircon (Table 3). Based on the high U–Pb isotopic closure temperature of zircon (e.g. Cherniak and Watson, 2000; Lee et al., 1997) and the topological features of the analysed grains, the U–Pb zircon date of 51.1 ± 1.0 Ma is regarded as the age of magmatic crystallization of the Gökseki leucogranodiorite. A slightly lower U–Pb zircon age of 47.7 ± 0.4 Ma was reported for the Gökseki leucogranodiorite by Özgülük et al. (2009). One zircon grain gave a nearly concordant U–Pb age of ~250–261 Ma (Late Permian). This grain is xenocrystic and is probably derived from Permo-Triassic accretionary complexes (Ağvanis Massif, Karakaya Complex), because these are the only units with late Permian ages in the Eastern Pontides (Topuz et al., 2004).

$^{40}Ar-^{39}Ar$ dating on hornblende and biotite separates from two samples (18A and 22A) of the Seme quartz diorite yielded well-defined plateau ages of ~51 Ma (Fig. 11, Table 4). The Ca/K ratios in the first degassing steps of both hornblende concentrates are relatively low. This is probably due to the presence of biotite inclusions (see chapter on petrography and mineral compositions). On the other hand, the Ca/K ratios of the biotites increase in the last degassing steps, probably caused by the presence of abundant apatite inclusions. Closure temperature values for Ar diffusion in hornblende and biotite are estimated to be 470–570 and 345–310 °C, respectively (Dahl, 1996; Grove and Harrison, 1996; Harrison et al., 1985). Since

22B–E	23B	10B	11B	16B	17B	17 C	19B	21B	23E	1093	1118
ME	A	DP	DP	DP	DP	DP	DP	DP	DP	LGR	LGR
Seme	Seme	Seme	Seme	Seme	Seme	Seme	Seme	Seme	Seme	Gökseki	Gökseki
50.91	75.61	69.10	66.96	68.47	67.08	62.30	69.43	70.60	62.87	70.98	71.23
1.36	0.07	0.26	0.39	0.26	0.38	0.67	0.27	0.28	0.61	0.29	0.23
15.90	13.43	16.41	16.85	15.35	16.68	17.69	16.47	15.46	16.36	16.14	15.81
8.76	0.30	1.86	2.56	2.10	2.56	4.47	1.92	1.88	3.91	1.36	1.65
0.16	0.04	0.03	0.03	0.04	0.08	0.03	0.04	0.06	0.01	0.02	
6.03	0.07	0.76	1.19	0.95	1.14	1.91	0.82	0.73	3.32	0.39	0.52
9.11	0.41	3.28	4.14	2.90	3.85	5.00	3.49	2.82	4.60	2.71	2.66
3.89	2.39	4.70	4.63	4.73	4.59	4.50	4.68	4.71	4.19	4.27	4.54
1.71	6.99	1.93	1.69	2.25	1.71	1.71	1.81	2.57	2.87	2.39	1.91
0.92	0.02	0.09	0.14	0.09	0.15	0.27	0.09	0.10	0.24	0.09	0.08
1.10	0.60	1.50	1.30	2.80	1.70	1.30	0.90	0.70	0.80	1.20	1.20
99.86	99.89	99.93	99.88	99.93	99.87	99.91	99.91	99.89	99.85	99.84	99.81
20	<1	4	5	4	5	8	4	3	11	1	<1
14.2	1.0	3.6	4.5	4.0	5.0	7.6	3.7	3.2	26.7	1.2	2.0
29.2	<0.5	4.2	6.7	4.4	5.6	10.5	4.2	3.8	15.0	1.8	2.6
246	<5	30	48	34	41	71	30	26	105	17	28
76.6	1.9	5.7	2.3	0.8	9	15.9	4.7	2.2	33.8	7.5	2.9
43	4	32	24	14	42	61	32	33	37	28	19
2.5	3.0	2.6	2.2	2.2	2.2	2.4	2.3	1.3	3.0	1.3	1.2
60	164	64	52	101	48	44	58	75	69	54	48
424.2	927	604	584	519	607	453	608	672	757	584	645
3.5	3.1	1.6	1.5	1.3	1.7	1.4	1.6	2.5	2.6	0.7	1.2
14.1	26.8	4.2	4.6	4.8	6.5	4.1	4.8	7.6	7.6	5.9	7.7
5.0	10.5	5.0	2.5	3.0	3.0	2.5	4.0	4.0	10.5	2.8	2.5
1010	619	635	824	574	784	798	649	694	862	613	605
24.2	3.1	4.1	5.4	4.1	5.9	8.8	4.1	6.7	9.3	9.4	10.0
1.2	0.2	0.3	0.3	0.3	0.3	0.5	0.3	0.4	0.6	0.5	0.6
69	85	96	110	86	122	132	94	127	110	129	127
2.4	3.1	2.6	3.2	2.3	3.1	3.7	2.9	3.4	3.2	3.6	3.4
26.4	1.7	5.2	5.4	4.7	6.4	13.4	5.2	6.5	11.1	4.4	6.7
22.3	11.4	17.2	19.7	16.2	20.0	21.1	18.0	19.0	19.6	17.7	16.7
48	7	7	34	14	21	7	14	14	48	14	14
73.0	19.2	13.1	21.0	12.1	23.3	20.2	13.2	21.3	25.3	15.6	19.7
172.8	24.0	26.4	42.6	23.7	46.3	47.5	25.3	42.1	51.7	30.4	37.5
23.02	1.76	2.79	4.55	2.57	5.04	5.83	2.71	4.44	5.70	3.44	3.69
88.4	4.9	9.8	15.1	8.8	17.0	21.8	9.0	14.2	20.6	13.2	12.9
12.20	0.50	1.60	2.20	1.50	2.30	3.80	1.60	2.10	3.20	1.99	1.81
2.82	0.20	0.46	0.66	0.42	0.69	1.14	0.49	0.56	0.93	0.68	0.61
8.48	0.45	1.32	1.60	1.22	1.80	3.49	1.33	1.71	2.85	1.59	1.45
1.15	0.06	0.20	0.23	0.18	0.23	0.54	0.19	0.25	0.43	0.17	0.18
5.79	0.30	1.12	1.12	0.96	1.39	2.85	1.11	1.27	2.33	1.01	1.15
0.98	<0.05	0.20	0.20	0.17	0.22	0.55	0.20	0.23	0.38	0.16	0.23
2.34	0.15	0.44	0.48	0.41	0.58	1.32	0.45	0.58	1.03	0.39	0.63
0.36	<0.05	0.09	0.08	0.07	0.09	0.17	0.06	0.08	0.14	0.05	0.11
2.13	0.19	0.49	0.46	0.45	0.57	1.10	0.47	0.57	0.97	0.29	0.64
0.32	0.03	0.08	0.07	0.06	0.08	0.18	0.08	0.09	0.15	0.05	0.11
0.44	2.92	0.41	0.37	0.48	0.37	0.38	0.39	0.55	0.68	0.56	0.42
57.66	31.59	44.71	47.91	47.23	46.84	45.81	45.80	43.45	62.69	36.20	38.41
0.64	1.10	1.04	0.99	0.99	1.02	0.96	1.03	0.99	0.89	1.11	1.10
23.11	68.13	18.02	30.78	18.13	27.56	12.38	18.93	25.19	17.58	36.27	20.75
0.85	1.29	0.97	1.08	0.95	1.04	0.96	1.03	0.90	0.94	1.17	1.15

(continued on next page)

the integrated and plateau age values of the hornblende and biotite concentrates are indistinguishable from each other within analytical uncertainty, these age values suggest rapid cooling between the respective closure temperatures of hornblende and biotite (~520 and 330 °C).

A biotite separate from a dacite porphyry cutting the metamorphic country rocks (sample 15B) yielded a well-defined plateau age of 51.2± 0.9 Ma (2σ, Fig. 11; Table 4). Due to the presence of abundant apatite inclusions in biotite, the Ca/K ratio increases towards the last degassing step.

To summarize, all the intrusive rocks exposed in the Ağvanis Massif were emplaced at ~51 Ma, i.e. during the Ypresian. Although the dacite porphyries are intrusive into both the Gökseki leucogranodiorite and the Seme quartz diorite, the relative age difference between the intrusive rocks is too small to be resolved by radiometric dating.

8. Sr–Nd isotopes

Measured and calculated initial (51 Ma) Sr and Nd isotopic compositions of selected samples from the Seme quartz diorite, Gökseki leucogranodiorite and dacite porphyries are listed in Table 5 and plotted in Fig. 12. Initial $^{87}Sr/^{86}Sr$ values [$^{87}Sr/^{86}Sr(i)$] range from 0.70421 to 0.70497 and $^{143}Nd/^{144}Nd(i)$ values range from 0.512514 to 0.512624. These values nearly correspond to those estimated for bulk

Table 2 *(continued)*

Samples	28B	29	1092B	1103A	1124	12	13	15B	47A	489
Rock type	LG	DP	DP	DP	DP	DP	DP	DP	DP	DP
Setting	Gökseki	Gökseki	Gökseki	Gökseki	Gökseki	Meta.	Meta.	Meta.	Meta.	Meta.
SiO_2	76.49	64.49	63.71	64.28	68.78	68.11	69.11	67.23	67.41	69.45
TiO_2	0.01	0.74	0.57	0.55	0.34	0.37	0.30	0.38	0.28	0.24
Al_2O_3	13.34	16.02	16.32	16.47	16.06	16.07	16.34	16.75	16.30	16.19
$Fe_2O_3^{tot}$	0.04	3.74	3.91	3.77	2.44	2.42	2.04	2.81	1.76	1.51
MnO	<0.01	0.06	0.07	0.06	0.05	0.03	0.03	0.05	0.03	0.02
MgO	0.06	2.12	1.82	2.17	1.40	1.28	0.95	1.08	1.06	0.69
CaO	0.87	3.96	4.48	3.73	3.87	3.77	3.41	3.92	3.51	3.09
Na_2O	3.87	3.85	3.78	4.40	4.60	4.48	4.72	4.55	4.03	4.81
K_2O	4.48	2.76	1.80	2.37	1.47	1.84	2.11	2.08	2.34	1.61
P_2O_5	<0.01	0.31	0.25	0.25	0.12	0.11	0.10	0.15	0.08	0.09
LOI	0.80	1.70	3.10	1.70	0.70	1.40	0.80	0.90	3.00	2.20
Total	99.94	99.73	99.78	99.74	99.81	99.89	99.92	99.90	99.83	99.87
Sc	<1	8	6	6	5	6	4	5	3	2
Ni	0.9	17.6	16.0	22.6	11.6	9.3	5.5	2.6	6.6	4.5
Co	0.5	10.3	6.3	10.2	6.5	7.4	5.4	6.2	4.6	4.7
V	13	107	76	74	52	50	39	39	42	36
Cu	4.9	35.5	1.9	14.9	4.8	19.8	26.8	9.7	21.3	15.4
Zn	5	51	70	39	40	15	19	37	37	25
Cs	0.6	2.6	1.9	2.2	1.6	1.7	1.5	1.9	1.1	0.5
Rb	87	55	47	63	37	52	58	63	43	33
Ba	463	718	657	609	577	639	651	605	654	395
U	1.0	3.0	1.0	3.0	1.0	1.0	1.0	1.0	1.0	1.0
Th	9.0	9.0	4.0	11.0	3.0	5.0	4.0	4.0	4.0	4.0
Pb	1.7	2.3	2.5	2.1	1.0	0.6	0.3	0.6	2.7	3.3
Sr	94	1058	815	814	653	643	658	658	646	628
Nb	4.3	6.2	7.4	11.4	5.6	5.2	4.8	6.4	3.8	4.1
Ta	0.3	0.5	0.5	0.7	0.3	0.3	0.4	0.4	0.3	0.3
Zr	42	122	102	136	103	111	98	115	72	87
Hf	2.6	4.0	3.0	3.4	2.4	2.9	2.6	3.0	2.2	2.2
Y	2.8	11.0	8.6	11.9	6.1	6.1	5.3	8.1	3.6	3.2
Ga	15.8	21.8	19.0	18.6	19.9	19.0	18.4	19.5	18.7	18.0
Cr	14	14	14	89	21	27	21	14	14	14
La	5.3	28.1	15.4	35.6	16.1	18.3	13.3	17.2	10.7	13.2
Ce	8.4	55.0	32.3	64.0	29.4	36.0	26.7	35.9	20.2	23.4
Pr	0.87	7.04	3.93	7.12	3.44	3.80	2.95	4.01	2.19	2.49
Nd	3.1	29.1	16.1	27.0	13.4	12.6	10.8	13.6	8.4	8.8
Sm	0.42	4.50	2.70	3.93	2.28	1.90	1.70	2.30	1.40	1.38
Eu	0.15	1.27	0.87	1.08	0.68	0.55	0.50	0.68	0.43	0.40
Gd	0.43	3.13	2.23	2.94	1.86	1.61	1.34	1.99	0.95	0.97
Tb	0.05	0.35	0.27	0.34	0.22	0.24	0.21	0.31	0.12	0.11
Dy	0.42	2.07	1.75	2.13	1.27	1.24	1.13	1.58	0.73	0.48
Ho	0.08	0.37	0.32	0.43	0.23	0.22	0.20	0.31	0.12	0.10
Er	0.27	0.96	0.91	1.22	0.62	0.55	0.49	0.72	0.35	0.28
Tm	0.05	0.15	0.13	0.18	0.09	0.09	0.08	0.13	0.04	0.05
Yb	0.43	0.95	0.78	1.06	0.49	0.51	0.49	0.78	0.30	0.25
Lu	0.08	0.14	0.12	0.17	0.08	0.07	0.07	0.12	0.05	0.04
K_2O/Na_2O	1.16	0.72	0.48	0.54	0.32	0.41	0.45	0.46	0.58	0.33
Mg#	74.90	52.87	47.94	53.25	53.27	51.14	47.96	43.20	54.37	47.48
ASI	1.04	0.97	1.00	0.99	0.99	0.99	1.01	0.99	1.05	1.06
$(La/Yb)_{cn}$	8.31	19.94	13.31	22.64	22.15	24.19	18.30	14.87	24.05	35.60
Eu/Eu*	1.08	1.03	1.08	0.97	1.01	0.96	1.01	0.97	1.14	1.06

earth and are similar to those of other adakitic plutons and volcanics of Early Eocene age and Middle Eocene high-K granitoids from the Eastern Pontides (Karslı et al., 2007, 2010; Topuz et al., 2005).

9. Depth of emplacement

The depth of emplacement of the Seme quartz diorite is constrained by (i) contact metamorphic mineral assemblages, (ii) Al-in-hornblende barometry and (iii) the occurrence of primary igneous epidote. Samples of contact metamorphic rocks taken at distances of <500 m from the contact to the Seme quartz diorite (e.g. samples 38 and 1155, Fig. 3) contain the mineral assemblages andalusite or garnet + biotite + muscovite + plagioclase + quartz. The presence of andalusite indicates a maximum pressure constraint of ~0.4 GPa (Bohlen et al., 1991; Holdaway and Mukhopadhyay, 1993; Pattison, 1992). Application of garnet–biotite Fe–Mg exchange thermometry and garnet–biotite–plagioclase–quartz barometry (Hoisch, 1990, 1991) yields 0.25–0.45 GPa and 550–600 °C.

Fig. 5. Harker variation diagrams for samples from the Seme quartz diorite, the Gökseki leucogranodiorite and dacitic porphyries. The diagram of K_2O vs SiO_2 shows field boundaries between medium-K (normal calc-alkaline), high-K and shoshonitic series of Peccerillo and Taylor (1976). QD: quartz diorite; ME: mafic enclave; A: aplite; LGR: leucogranodiorite; LG: leucogranite; and DP: dacite porphyry.

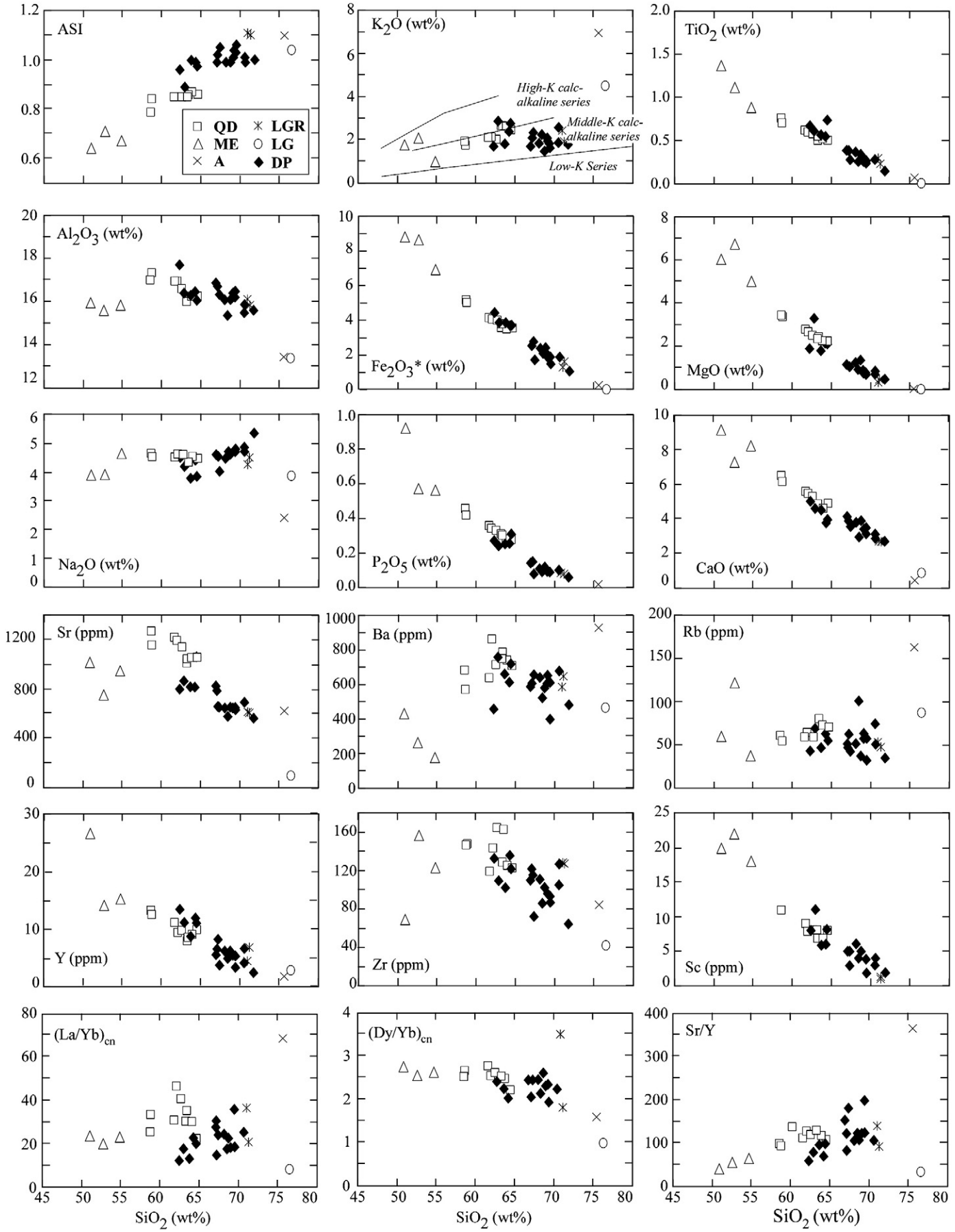
ASI
QD
ME
A
LGR
LG
DP
K2O (wt%)
High-K calc-alkaline series
Middle-K calc-alkaline series
Low-K Series
TiO2 (wt%)
Al2O3 (wt%)
Fe2O3* (wt%)
MgO (wt%)
Na2O (wt%)
P2O5 (wt%)
CaO (wt%)
Sr (ppm)
Ba (ppm)
Rb (ppm)
Y (ppm)
Zr (ppm)
Sc (ppm)
(La/Yb)cn
(Dy/Yb)cn
Sr/Y
SiO2 (wt%)
SiO2 (wt%)
SiO2 (wt%)

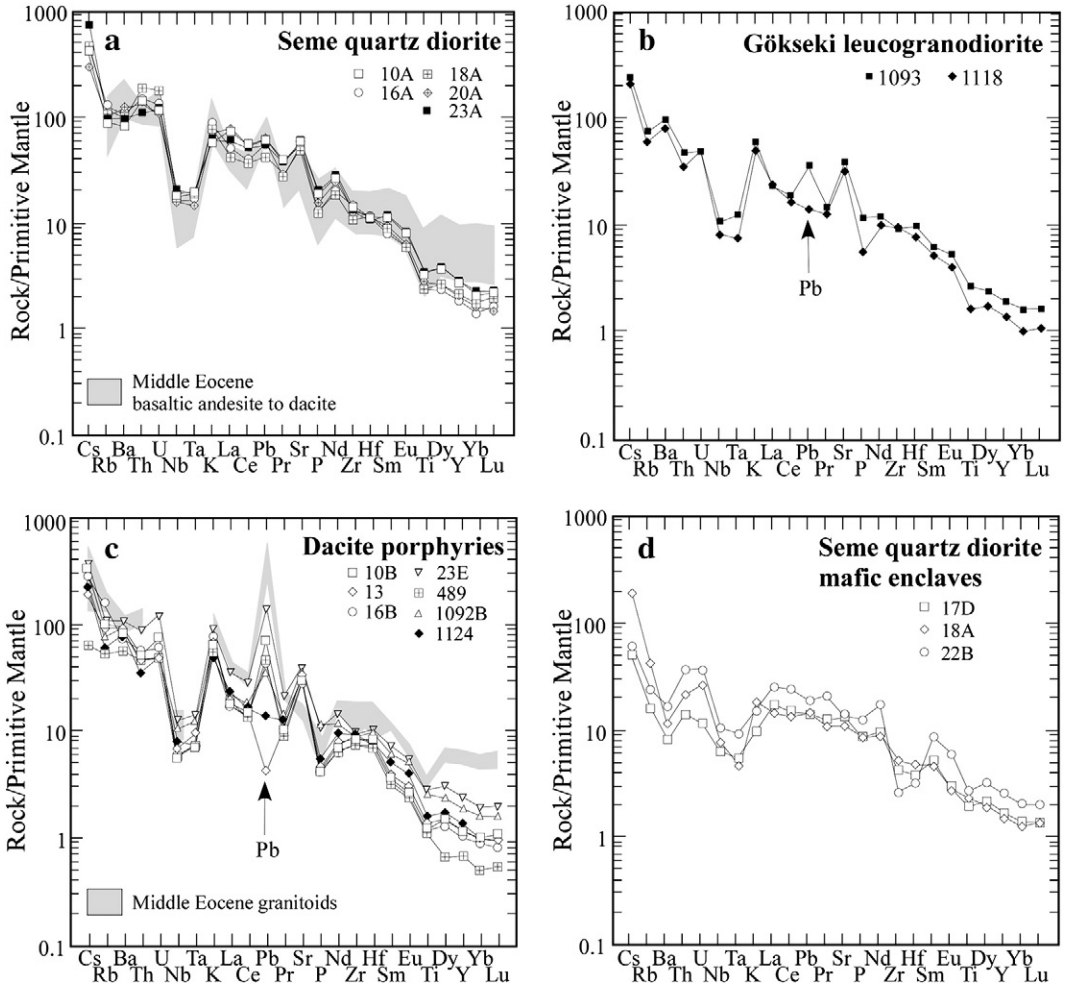

Fig. 6. Primitive mantle-normalized trace element abundance patterns (normalized to values given in Sun and McDonough, 1989). Data on Middle Eocene granitoids and basaltic andesite to dacitic volcanics from Karslı et al. (2007) and Kaygusuz et al. (2011).

The Seme quartz diorite contains the critical mineral assemblage hornblende + biotite + plagioclase + K-feldspar + quartz + titanite + Ti-magnetite + apatite that together with melt allows for the application of the Al-in-hornblende barometer (Anderson and Smith, 1995, and references therein). Hornblende in the quartz diorite displays nearly constant Al_2O_3 contents of 7.3–9.1 wt.% (Table 1). Rim compositions of hornblende in contact with quartz and K-feldspar are used for estimating the pressure at which late-stage crystallization of the magma has occurred. Using the calibration of Anderson and Smith (1995) and assuming a solidus temperature of 700 °C, pressures of 0.34–0.45 GPa are obtained. Finally, the presence of primary (igneous) epidote (ps_{87-93}) in the quartz diorite also argues for minimum pressures of 0.3–0.4 GPa (Schmidt and Poli, 2004, and references therein). It is, therefore, suggested that the Seme quartz diorite was emplaced at a depth of ~13–16 km.

The depth of emplacement of the Gökseki leucogranodiorite is unconstrained due to the absence of pressure-sensitive mineral assemblage in the contact metamorphic samples and lack of hornblende in the granodiorite. Porphyric texture in the dacitic dikes implies that crystallization has occurred at two distinct stages whereby the last stage occurred at rather shallow depths. Depth assignment to the last stage of crystallization is fraught with large uncertainties. Conservatively, a depth ≤7 km can be assumed. On the other hand, the hornblende phenocrysts in the porphyries display rather elevated Al_2O_3 contents (10–15 wt.%; Table 1), which would argue for elevated pressures. Although all the phases required for the application of Al-in-hornblende barometry are present in the porphyries, equilibrium among all the phases cannot be unequivocally assumed.

10. Discussion

10.1. Fractional crystallization

In many Harker diagrams, the samples from the Seme quartz diorite, the Gökseki leucogranodiorite and the dacite porphyries define roughly similar trends (Fig. 5). Based on the identical Sr–Nd isotope composition and coeval ages, the linear trends on the Harker diagrams suggest that these rocks may be genetically related. Initial ε_{Nd} and $^{87}Sr/^{86}Sr$ values of the Seme quartz diorite and the dacite porphyries display no unequivocal correlation with SiO_2 (not shown), suggesting that crustal contamination or assimilation was insignificant.

None of the rocks has a significant negative Eu anomaly and primitive mantle-normalized element concentration diagrams show positive Sr anomalies. These characteristics argue against fractionation of plagioclase. On the other hand, the highly fractionated REE patterns (high La/Yb ratios) together with the overall low abundances of Y and HREE require the presence of garnet as a fractionating or residual phase. The Sr/Y and La/Yb ratios of the dacite porphyries correlate weakly with increasing SiO_2 (Fig. 5). In addition, abundances of Y, Yb and Sc decrease with increasing SiO_2, suggesting that the adakitic signature becomes more pronounced as mineral fractionation (e.g. garnet, hornblende and clinopyroxene) increases. The Seme

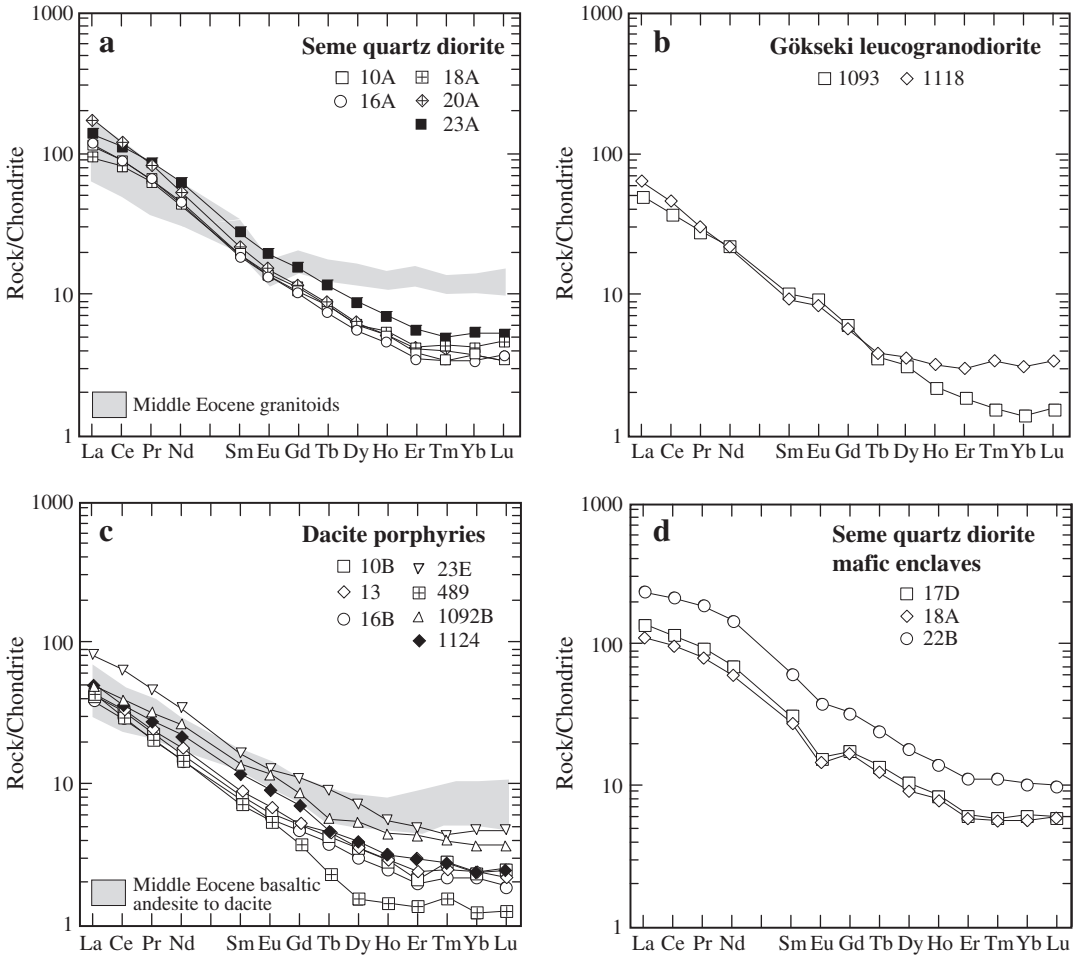

Fig. 7. Chondrite-normalized rare earth element abundance patterns (normalized to values given in Boynton, 1984). Data on Middle Eocene granitoids and basaltic andesite to dacitic volcanics from Karslı et al. (2007) and Kaygusuz et al. (2011).

quartz diorites and the dacite porphyries form discrete compositional trends, ruling out a relationship via fractional crystallization. The Dy/Yb ratios slightly correlate with increasing SiO_2, indicating that fractionation of amphibole was more important than that of garnet. Negative P anomalies in primitive-mantle normalized concentration diagrams and decreasing P_2O_5 with increasing SiO_2 indicate apatite fractionation. Based on the above arguments we infer a fractionating and/or residual mineral assemblage of hornblende, garnet, clinopyroxene and apatite without significant involvement of plagioclase. To summarize, the three groups of rocks represent melts generated from a similar source by variable degrees of partial melting and different degrees of fractional crystallization.

10.2. Origin of adakitic signatures

There has been a great deal of confusion about the term 'adakite' (defined by Defant and Drummond, 1990) during the last years. According to Moyen (2009), this term should only be used for the 'high-silica adakites' (HSA) as defined by Martin et al. (2005). This definition not only includes a number of geochemical characteristics, such as high Sr (~300–1300 ppm), low Y (<18 ppm), high Sr/Y (>40), low Yb (<1.9 ppm), high $(La/Yb)_{cn}$ (>10), $Eu/Eu^* \approx 1$, low Sc (<20 ppm), low K_2O/Na_2O (<0.6), relatively high Mg# values (~35–60) and high Al_2O_3 (>15.5 wt.%), but is also restricted to subduction-related rocks. The latter part of this definition, however, is problematic, since the role of the subduction process in the genesis of adakites is by no means clear. Melts with adakitic signatures may be produced by (i) slab melting and subsequent slab melt–mantle interactions (the 'classical model'; Defant and Drummond, 1990), (ii) fractionation of garnet + amphibole from 'normal' partial melts generated in the mantle wedge, and (iii) partial re-melting of solidified arc basalt containing garnet + amphibole in the lower parts of a thickened crust (e.g. Alonso-Perez et al., 2009; Atherton and Petford, 1993; Chiaradia et al., 2009; Macpherson et al., 2006; Petford and Atherton, 1996).

The 'classical model' for the generation of adakitic melts faces a number of difficulties, the most important one being the question how melting can proceed in a cold slab (e.g. Peacock et al., 1994). In addition, it is difficult for 'slab-produced' high-silica adakitic melts to reach the surface, because they would quickly freeze within the peridotite mantle (Yaxley and Green, 1998). Moreover, the oceanic lithosphere is very heterogeneous in $\delta^{18}O$ (e.g. Staudigel et al., 1995) and displays depleted Sr–Nd isotopic signatures (e.g. Macpherson et al., 2006). Similar diversity would be predicted for melts derived from subducted slabs. Oxygen and Sr–Nd isotope compositions of a wide variety of subduction-related adakites, however, give little evidence of a supposed slab component (Bindeman et al., 2005; Macpherson et al., 2006).

If high-silica adakitic melts are not produced by slab melting, but rather represent products from the upper plate, it is also possible to generate such melts in the aftermath of subduction and collision. Since adakitic signatures with low K_2O/Na_2O ratios (<0.6) were recently also discovered in post-collisional igneous rocks (Castillo, 2008; Topuz et al., 2005; Wang et al., 2006), the linkage of adakitic melts to slab melting is no longer mandatory. Instead, partial melting of a garnet-bearing mafic lower crust has been promoted as a model

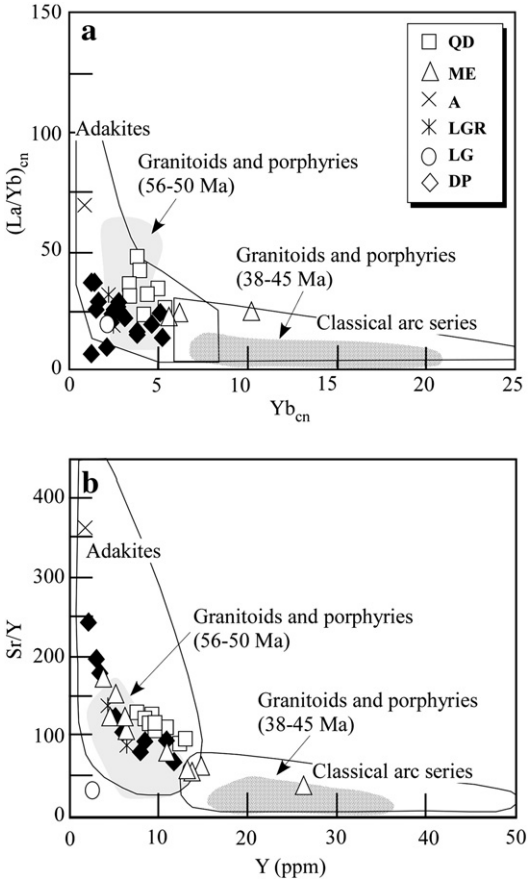

Fig. 8. Adakite discrimination diagrams (a) $(La/Yb)_{cn}$ vs Yb_{cn} (b) Sr/Y vs Y. QD: quartz diorite; ME: mafic enclave; A: aplite; LGR: leucogranodiorite; LG: leucogranite; and DP: dacite porphyry.

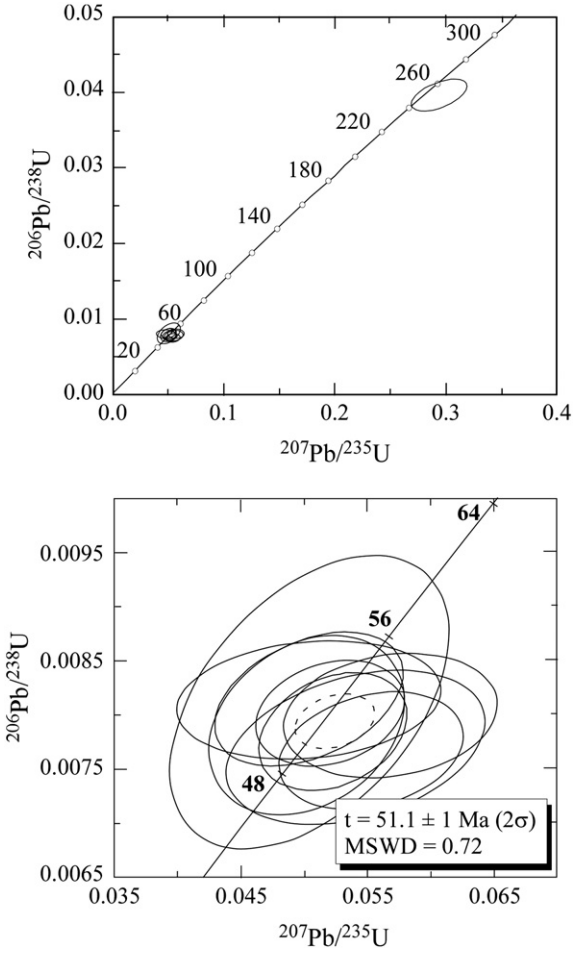

Fig. 10. Concordia diagrams of LA–ICP–MS U–Pb zircon ages from the Gökseki leucogranodiorite. Error ellipses are given at the 2σ level. Concordia ages calculated by Isoplot 3.50 (Ludwig, 2003).

for the production of adakitic melts (e.g. Chiaradia et al., 2009; Macpherson et al., 2006; Topuz et al., 2005; Wang et al., 2006). Parts of the lower crust above a subduction zone may be formed by underplated basic melts, crystallized as garnet-amphibole-bearing rocks.

Melt fractions and compositions produced by melting of a primitive basaltic source (Mg#≈70) at given *P* and *T* will strongly depend on the amount of H_2O available in the system. Unfortunately, most experiments performed so far have been carried out on MORB-like systems with low potassium contents and Mg# values significantly less than 70 (e.g. López and Castro, 2001; Prouteau and Scaillet, 2003; Rapp, 1995; Rapp and Watson, 1995; Rapp et al., 1991; Şen and Dunn, 1994; Winther, 1996; Winther and Newton, 1991). However, Alonso-Perez et al. (2009) performed a number of partial melting experiments on an andesitic composition (Mg# = 40) at pressures of 0.8 to 1.2 GPa. The experiments at 1.2 GPa showed that at relatively high H_2O contents in the liquid, garnet + amphibole are the high-temperature liquidus phases, followed by plagioclase at lower temperature. Fractionation of garnet, in addition to its influence on the trace element (Y, HREE and Sc) characteristics of derivative

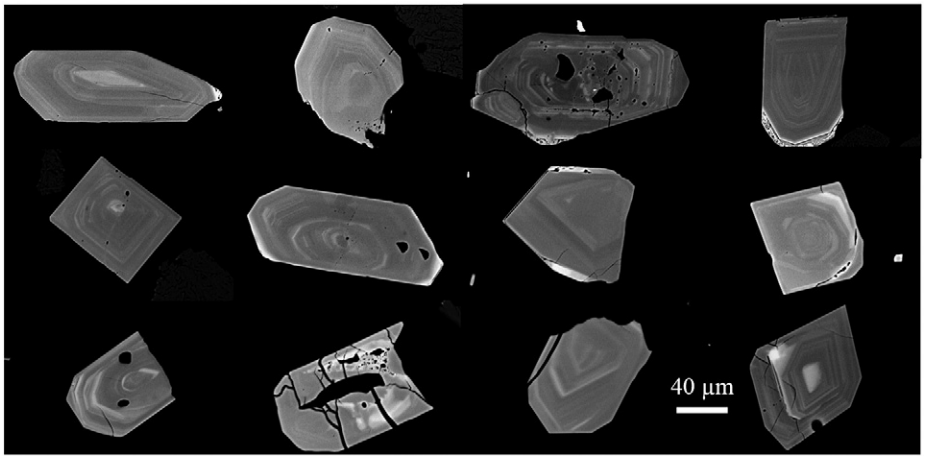

Fig. 9. Back-scattered electron images of zircons from the Gökseki leucogranodiorite (sample 28).

Table 3
LA–ICP–MS U–Th–Pb isotopic data and calculated ages for zircon grains from the Gökseki leucogranodiorite, Ağvanis Massif, NE Turkey.

Analysis	Th	U	Th/U	$^{206}Pb/^{204}Pb$	$^{207}Pb/^{235}U$	$^{206}Pb/^{238}U$	rho	$^{207}Pb/^{206}Pb$	$^{208}Pb/^{232}Th$	$^{208}Pb/^{232}Th$	$^{207}Pb/^{235}U$	$^{206}Pb/^{238}U$
Session I (spot size 35 μm)												
58	530	664	0.80	>519	0.055(03)	0.0077(02)	0.26	0.0521(028)	0.0024 (01)	49.4 ± 2.1	54.7 ± 2.9	49.3 ± 1.4
59	209	491	0.43	>372	0.057(03)	0.0080(02)	0.18	0.0514(032)	0.0029 (01)	58.4 ± 2.4	56.1 ± 3.3	51.3 ± 1.5
60*	269	523	0.51	74	0.430(30)	0.0108(03)	0.24	0.2883(199)	0.0151(10)	303 ± 21	363 ± 21	69 ± 2
61	737	1034	0.71	>810	0.052(02)	0.0078(02)	0.29	0.0482(022)	0.0024(01)	49.3 ± 2.0	51.7 ± 2.3	50.4 ± 1.4
63	321	616	0.52	>569	0.050(03)	0.0079(03)	0.27	0.0459(030)	0.0026(01)	53.1 ± 2.7	49.7 ± 3.1	50.8 ± 2.2
64	438	725	0.60	>604	0.052(02)	0.0080(02)	0.25	0.0469(022)	0.0025(01)	50.0 ± 1.9	51.5 ± 2.3	51.5 ± 1.3
Session II (spot size 27 μm)												
34	320	737	0.43	>1425	0.294(10)	0.0396(09)	0.56	0.0538(016)	0.0143(04)	286 ± 8	261 ± 8	250 ± 5
35	521	499	1.04	>209	0.050(05)	0.0081(06)	0.46	0.0450(038)	0.0025(03)	49.9 ± 6.7	50.0 ± 4.4	52.1 ± 3.5
36*	494	594	0.83	276	0.065(04)	0.0080(02)	0.27	0.0590(036)	0.0026(01)	52.9 ± 2.2	64.2 ± 4.0	51.5 ± 1.3
37	357	537	0.66	>214	0.054(04)	0.0077(03)	0.33	0.0509(038)	0.0027(02)	54.5 ± 3.8	53.4 ± 4.0	49.5 ± 1.9
38	307	462	0.66	>223	0.050(04)	0.0081(02)	0.17	0.0449(038)	0.0025(02)	51.4 ± 2.5	49.9 ± 4.1	52.3 ± 1.4
39	267	679	0.39	196	0.050(03)	0.0081(03)	0.39	0.0448(025)	0.0028(02)	57.4 ± 3.3	49.9 ± 2.9	52.3 ± 1.6
40*	870	842	1.03	150	0.118(10)	0.0088(03)	0.26	0.0977(078)	0.0045(03)	91 ± 7	114 ± 9	56 ± 2
41*	117	305	0.38	117	0.249(56)	0.0094(04)	0.07	0.1923(433)	0.0122(26)	244 ± 52	225 ± 46	60 ± 3

U and Th concentrations are estimated from sensitivity factors calculated from GJ zircon (the Mainz crystal has 322 ppm U and 10.7 ppm Th). ^{204}Hg interferences on ^{204}Pb are subtracted using a $^{201}Hg/^{204}Hg$ ratio of 1.918. ^{235}U is calculated from ^{238}U using a $^{238}U/^{235}U$ ratio of 137.88. rho = error correlation defined as the quotient of the propagated errors of the $^{206}Pb/^{238}U$, $^{207}Pb/^{235}U$ and $^{207}Pb/^{206}Pb$ ratios. Uncertainties in parentheses are given for the last two digits and correspond to 1σ.
* = Analysis not used for age calculation, due to irregular behaviour of the ablation signal.

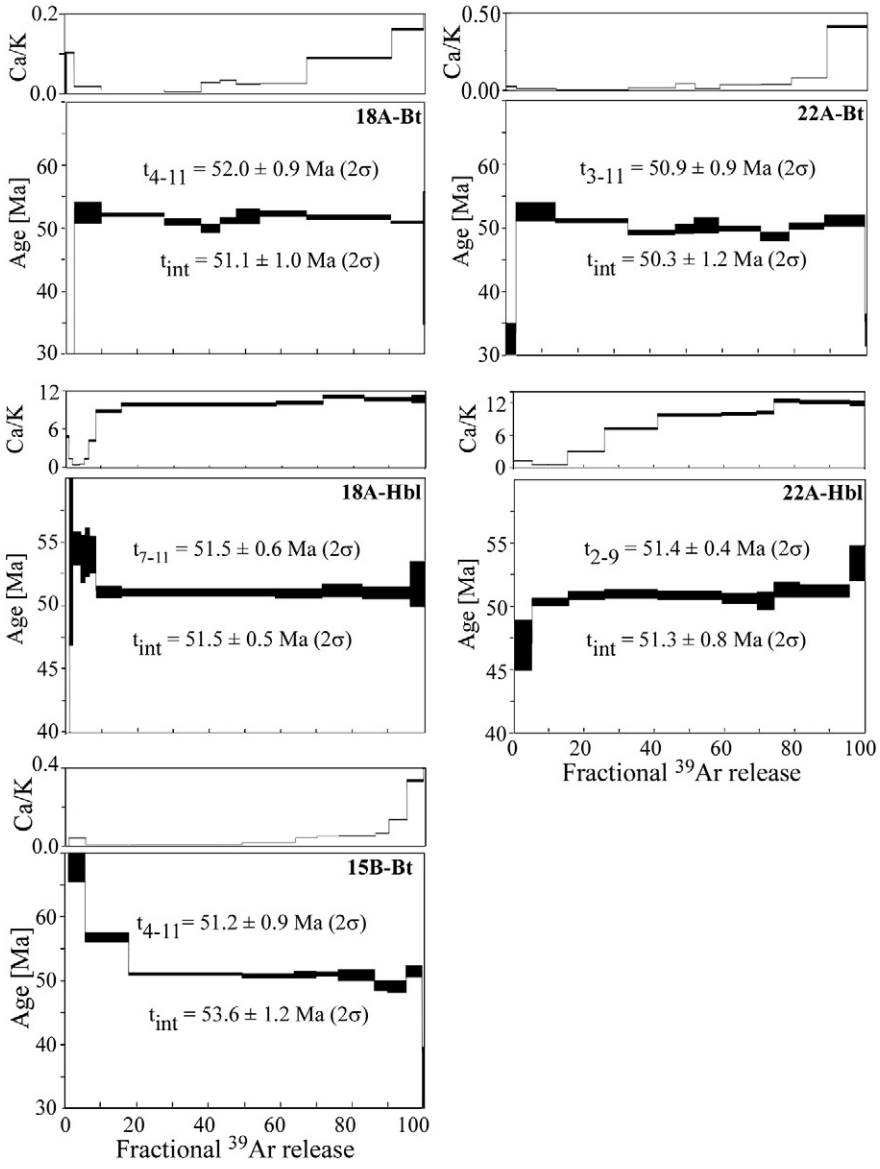

Fig. 11. $^{40}Ar/^{39}Ar$ incremental spectra of biotite and hornblende separate.

Table 4
Ar–Ar data for biotite and hornblende separates from the intrusive rocks in the Ağvanis Massif, NE Turkey.

Step	T (°C)	$^{37}Ar/^{39}Ar$	$^{40}Ar^*/^{39}Ar$	^{39}Ar (%)	Age (Ma)
*15 Bt (J = 52.56 ± 0.24 (0.46)) * 10^{-4}*					
1	500	0 ± 0	15.3 ± 4.2	0.98	140 ± 37 (37)
2	580	0.0213 ± 0.0020	7.54 ± 0.93	4.69	70 ± 8 (8)
3	630	0.0040 ± 0.0002	6.13 ± 0.18	12.12	57.2 ± 1.7 (1.7)
4	670	0.0037 ± 0.0002	5.50 ± 0.04	31.45	51.44 ± 0.43 (0.57)
5	710	0.0098 ± 0.0004	5.47 ± 0.07	14.71	51.14 ± 0.66 (0.78)
6	750	0.0220 ± 0.0010	5.49 ± 0.11	6.09	51.4 ± 1.0 (1.1)
7	820	0.0265 ± 0.0012	5.50 ± 0.07	6.04	51.41 ± 0.67 (0.77)
8	890	0.0268 ± 0.0010	5.47 ± 0.18	10.10	51.2 ± 1.7 (1.7)
9	940	0.0346 ± 0.0016	5.30 ± 0.18	3.76	49.6 ± 1.7 (1.8)
10	1000	0.0715 ± 0.0030	5.28 ± 0.20	5.09	49.4 ± 1.9 (1.9)
11	1060	0.176 ± 0.007	5.54 ± 0.19	4.45	51.8 ± 1.7 (1.8)
12	1200	3.52 ± 0.14	3.2 ± 2.0	0.45	31 ± 19 (19)
13	1400	3.15 ± 0.50	4 ± 20	0.05	41 ± 183 (183)
Total		0.0398 ± 0.0018	5.73 ± 0.12	100.00	53.6 ± 1.1 (1.2)
*18A Bt (J = 52.87 ± 0.39 (0.55)) * 10^{-4}*					
1	400	0 ± 0	8 ± 18	0.15	75 ± 166 (166)
2	500	0.0541 ± 0.0022	1.43 ± 0.75	2.24	13.6 ± 7.1 (7.1)
3	580	0.0097 ± 0.0004	5.62 ± 0.37	7.56	52.8 ± 3.5 (3.5)
4	630	0.0050 ± 0.0002	5.58 ± 0.05	17.55	52.42 ± 0.63 (0.74)
5	660	0.0027 ± 0.0002	5.46 ± 0.12	10.28	51.3 ± 1.2 (1.2)
6	690	0.0153 ± 0.0008	5.35 ± 0.15	5.26	50.3 ± 1.5 (1.5)
7	730	0.0180 ± 0.0016	5.47 ± 0.12	4.42	51.5 ± 1.2 (1.2)
8	800	0.0130 ± 0.0014	5.54 ± 0.26	6.62	52.1 ± 2.4 (2.4)
9	870	0.0135 ± 0.0006	5.60 ± 0.11	12.91	52.6 ± 1.1 (1.1)
10	980	0.0472 ± 0.0022	5.54 ± 0.06	23.57	52.06 ± 0.66 (0.76)
11	1200	0.0850 ± 0.0034	5.45 ± 0.03	9.06	51.26 ± 0.47 (0.60)
12	1400	0.188 ± 0.011	4.9 ± 2.3	0.39	46 ± 21 (21)
Total		0.0269 ± 0.0012	5.44 ± 0.10	100.00	51.1 ± 1.0 (1.0)
*18A Hbl (J = 50.85 ± 0.26 (0.48)) * 10^{-4}*					
1	500	2.51 ± 0.19	1.8 ± 4.5	0.78	16 ± 40 (40)
2	600	0.708 ± 0.067	6.1 ± 1.7	1.02	55 ± 16 (16)
3	700	0.220 ± 0.033	6.09 ± 0.29	2.00	55.0 ± 2.6 (2.6)
4	760	0.294 ± 0.051	6.00 ± 0.42	1.28	54.2 ± 3.8 (3.8)
5	820	0.71 ± 0.10	6.05 ± 0.42	1.32	54.7 ± 3.8 (3.8)
6	880	2.17 ± 0.14	6.04 ± 0.33	1.86	54.5 ± 3.0 (3.0)
7	940	4.57 ± 0.26	5.70 ± 0.11	7.10	51.6 ± 1.0 (1.1)
8	1000	5.11 ± 0.28	5.699 ± 0.070	43.08	51.54 ± 0.64 (0.80)
9	1060	5.24 ± 0.30	5.688 ± 0.094	13.11	51.44 ± 0.84 (0.92)
10	1120	5.75 ± 0.34	5.71 ± 0.11	11.45	51.7 ± 1.0 (1.1)
11	1200	5.53 ± 0.33	5.70 ± 0.11	13.32	51.5 ± 1.0 (1.1)
12	1300	5.54 ± 0.65	5.77 ± 0.40	3.67	52.2 ± 3.6 (3.6)
Total		4.89 ± 0.14	5.697 ± 0.058	100.00	51.52 ± 0.52 (0.64)
*22A Bt (J = 52.97 ± 0.19 (0.43)) * 10^{-4}*					
1	400	0 ± 0	12 ± 23	0.18	108 ± 205 (205)
2	500	0.0126 ± 0.0024	3.1 ± 1.2	2.61	30 ± 11 (11)
3	580	0.0048 ± 0.0014	5.63 ± 0.32	11.05	53.0 ± 3.0 (3.0)
4	620	0.0020 ± 0.0002	5.47 ± 0.06	19.91	51.54 ± 0.62 (0.73)
5	650	0.0086 ± 0.0006	5.27 ± 0.07	12.93	49.65 ± 0.68 (0.77)
6	700	0.0221 ± 0.0010	5.34 ± 0.16	5.46	50.4 ± 1.5 (1.5)
7	760	0.0052 ± 0.0008	5.39 ± 0.26	6.66	50.8 ± 2.4 (2.4)
8	840	0.0186 ± 0.0008	5.34 ± 0.09	11.63	50.27 ± 0.89 (0.96)
9	900	0.0199 ± 0.0008	5.20 ± 0.17	8.08	49.1 ± 1.7 (1.7)
10	1060	0.0412 ± 0.0016	5.37 ± 0.12	9.62	50.6 ± 1.1 (1.2)
11	1200	0.216 ± 0.009	5.47 ± 0.19	11.26	51.6 ± 1.8 (1.8)
12	1400	1.287 ± 0.053	3.61 ± 0.54	0.61	34.2 ± 5.0 (5.0)
Total		0.0438 ± 0.0020	5.34 ± 0.12	100.00	50.3 ± 1.1 (1.2)
*22A Hbl (J = 51.01 ± 0.10 (0.40)) * 10^{-4}*					
1	600	0.668 ± 0.040	5.22 ± 0.44	5.26	47 ± 4 (4)
2	800	0.291 ± 0.019	5.600 ± 0.073	10.29	50.82 ± 0.66 (0.76)
3	900	1.543 ± 0.090	5.658 ± 0.073	10.37	51.33 ± 0.66 (0.76)
4	950	3.77 ± 0.22	5.672 ± 0.077	15.08	51.46 ± 0.70 (0.79)
5	970	5.10 ± 0.29	5.661 ± 0.078	18.39	51.36 ± 0.71 (0.80)
6	990	5.21 ± 0.31	5.634 ± 0.093	9.87	51.12 ± 0.84 (0.92)
7	1020	5.34 ± 0.34	5.61 ± 0.16	4.90	50.9 ± 1.4 (1.4)
8	1080	6.49 ± 0.40	5.71 ± 0.14	7.35	51.8 ± 1.3 (1.3)
9	1180	6.36 ± 0.39	5.70 ± 0.11	14.25	53.9 ± 1.4 (1.4)
10	1300	6.23 ± 0.52	5.95 ± 0.32	4.27	51.7 ± 1.0 (1.1)
Total		4.155 ± 0.095	5.650 ± 0.041	100.00	51.26 ± 0.37 (0.52)

Notes to Table 4:
Uncertainties are ± 2σ. Errors in parentheses comprise age error and uncertainty of standard. The in-house standard'Bmus/2′ (Bärhalde muscovite) was used; age is 328.5 ± 2.2 Ma (2σ). (Schwarz and Trieloff, 2007).

Table 5
Sr–Nd isotope ratios of the Seme quartz diorite, Gökseki leucogranodiorite and dacite porphyries from the Ağvanis Massif, NE Turkey.

Sample	$^{87}Rb/^{86}Sr$	$^{87}Sr/^{86}Sr$	$^{87}Sr/^{86}Sr(i)$	$^{143}Nd/^{144}Nd$	$^{143}Nd/^{144}Nd(i)$	ε_{Nd} (i)	T_{DM}
Seme quartz diorite							
11A	0.1396	0.704809 (09)	0.70471	0.512586 (10)	0.512559	−0.3	0.88
17A	0.2311	0.704842 (08)	0.70468	0.512594 (19)	0.512566	−0.1	0.87
18A	0.1937	0.704815 (09)	0.70467	0.512601 (10)	0.512571	0.0	0.86
22A	0.1418	0.704862 (08)	0.70476	0.512567 (11)	0.512537	−0.7	0.92
Mafic enclaves							
17D	0.1136	0.704760 (06)	0.70468	0.512604 (07)	0.512575	0.0	0.86
22B	0.1718	0.704854 (09)	0.70473	0.512562 (11)	0.512534	−0.7	0.92
Aplite							
23B	0.7664	0.705521 (06)	0.70497	0.512535 (07)	0.512514	−1.1	0.95
Gökseki leucogranodiorite							
1093	0.2548	0.704978 (09)	0.70479	0.512624 (05)	0.512593	0.4	0.83
1118B	0.2295	0.704821 (10)	0.70465	0.512652 (06)	0.512624	1.0	0.78
Dacite porphyries							
11B	0.1825	0.705044 (09)	0.70491	0.512555 (08)	0.512525	−0.9	0.94
15A	0.2769	0.704343 (09)	0.70421	n.a.	–	–	–
17B	0.1771	0.705067 (09)	0.70494	0.512555 (07)	0.512528	−0.9	0.93
23E	0.2315	0.704572 (09)	0.70440	0.512586 (54)	0.512555	−0.3	0.89

Uncertainties for the $^{87}Sr/^{86}Sr$ and $^{143}Nd/^{144}Nd$ ratios are $2s_m$ errors in the last two digits (in parantheses). Initial values are calculated for an assumed age of 51 Ma. $\varepsilon_{Nd}(i)$ values are calculated relative to CHUR with present day values of $^{143}Nd/^{144}Nd = 0.512638$ and $^{147}Sm/^{144}Nd = 0.1967$ (Jacobsen and Wasserburg, 1980). Nd model ages (T_{DM}) are calculated with a depleted-mantle reservoir and present-day values of $^{143}Nd/^{144}Nd = 0.513151$ and $^{147}Sm/^{144}Nd = 0.219$ (e.g. Liew and Hofmann, 1988).

liquids, has the effect of increasing Mg# values and SiO_2 contents of coexisting liquids, and hence tends to produce high-Mg liquids. This behaviour is opposite to that of amphibole, which has a considerably lower Fe/Mg solid/liquid partition coefficient (~0.40 for amphibole vs 0.85 for garnet, at ~1.2 GPa). For more mafic compositions (Mg# ≈ 70), pressures of more than 1.2 GPa and high H_2O contents are necessary to stabilize garnet + amphibole as near-liquidus phases (Müntener et al., 2001).

Summarizing, adakitic melts could be produced from primitive 'normal' arc basalts that either undergo fractional crystallization (garnet + amphibole) during ascent, or transport the heat necessary to remelt older crystallized basic rock in the lowermost continental crust. In any case, interaction between adakitic magma and mantle peridotite seems to be possible (Chiaradia et al., 2009; Macpherson et al., 2006).

10.3. Exhumation of the Ağvanis Massif during the Late Paleocene to Middle Eocene

Similar isotopic ages (~51 Ma) combined with different emplacement depths of 13–16 km and ≤7 km for the Seme quartz diorite and the dacite porphyries, respectively, indicate high exhumation rates (≥0.6 cm a^{-1}) in the Early Eocene (ca. 51 Ma) during the intrusion of the magmatic rocks. Locally well-developed foliation indicates penetrative strain during the exhumation. Boztuğ et al. (2004) inferred high uplift rates (>0.1 cm a^{-1}) for the Late Paleocene-Early Eocene period (57–47 Ma), based on the apatite fission track data from several granites in the Eastern Pontides. During the same period, the southern zone of the Eastern Pontides close to the collision front underwent a significant shortening (crustal thickening) as indicated

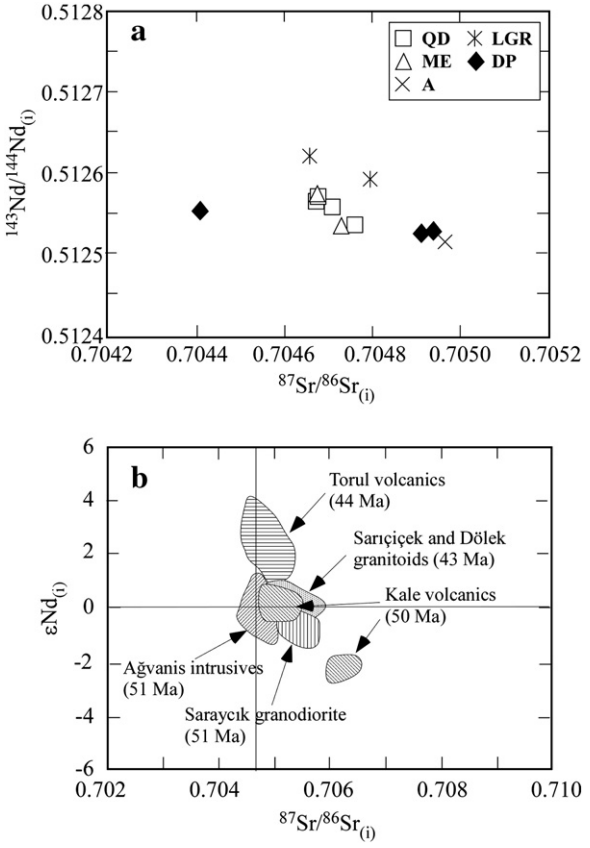

Fig. 12. Variation of (a) initial $^{87}Sr/^{86}Sr$ vs initial $^{143}Nd/^{144}Nd$ values. QD: quartz diorite; ME: mafic enclave; A: aplite; LGR: leucogranodiorite; DP: dacite porphyry. (b) Sr–Nd isotopic compositions of the Eocene igneous rocks from the Eastern Pontides. Data from Topuz et al. (2005), Karslı et al. (2007, 2010), and Kaygusuz et al. (2011).

by several north-vergent thrust slices (Okay and Şahintürk, 1997; Okay et al., 1997). Consequently, high exhumation rate was associated with crustal shortening and high uplift.

The metamorphic rocks of the Ağvanis Massif and the late Paleocene olistostromal sequence to the northeast (Fig. 4) are unconformably overlain by Middle Eocene (Early Lutetian ca. 46 Ma) sedimentary rocks (Pelin, 1977), suggesting that the adakitic intrusives were at or very near the Earth's surface by the Middle Eocene. However, subsidence below sea level and probably last stage exhumation was related to extentional tectonics (see below).

10.4. Causes of Eocene magmatism in Northern Turkey

Recent studies show that the Early Eocene granitoids and andesitic to dacitic volcanics in the Eastern Pontides display adakitic signatures (e.g. Eyüboğlu et al., 2011a, 2011b; Karslı et al., 2010; Topuz et al., 2005). This adakitic signature disappears in the Middle to Late Eocene granitoids and porphyries that are characterized by moderately fractionated REE patterns with $(La/Yb)_{cn} \approx 4–10$ and significant negative Eu anomalies ($Eu/Eu^* = 0.50–0.80$) as well as by high abundances of Y (>15 ppm) and low Sr/Y ratios (<40) (Arslan and Aslan, 2006; Boztuğ, 2008; Boztuğ et al., 2006, 2007; Karslı et al., 2007). Such geochemical features are indicative of a fractionating/residual mineral assemblage consisting of plagioclase, hornblende and pyroxene without involvement of significant amounts of garnet. Except for plagioclase- and garnet-compatible elements (e.g., Sr, Eu, Y and HREEs), incompatible trace element ratios and Sr–Nd isotopic signatures of the Early Eocene adakitic rocks and Middle Eocene granitoids are similar (Figs. 6, 7 and 12b), suggesting derivation from similar sources. On the other hand, the Middle Eocene volcanics only differ from the adakitic rocks in the slightly fractionated nature of the REE patterns (Figs. 6 and 7).

A critical assessment of the literature data on Tertiary granitoids from Turkey reveals that the abrupt temporal change in the geochemical features of the granitoids, e.g. $(La/Yb)_{cn}$, Eu/Eu*, Sr/Y, Y and Yb, is also valid for the granitoids in the western Pontides and those closely located to the south of the İzmir–Ankara–Erzincan and Intra-Tauride sutures, albeit not so pronounced as in the Eastern Pontides (Fig. 1a). The Paleocene to Early Eocene granitoids of Cavuşoğlu (~64 Ma), Horoz (~54 Ma; Kadıoğlu and Dilek, 2010; Kuşçu et al., 2010) and Sivrihisar (~54 Ma; Kibici et al., 2008) display either adakitic signature or signatures transitional to adakite. In marked contrast, the Middle to Late Eocene granitoids in the western Pontides and the Tavşanlı Zone (Topuk, Kapıdağ and Karabiga granitoids) do not show an adakitic flavor (Altunkaynak, 2007; Harris et al., 1994; Karacık et al., 2008; Ustaömer et al., 2009).

Paleocene to Early Eocene adakite-like magmatism is restricted to the Pontides and the northernmost part of the Anatolide–Tauride block, and is post-collisional with respect to the Izmir–Ankara–Erzincan suture (Fig. 1). The present distance between the known adakite locations and the Bitlis–Zagros suture is about 250 km, but was significantly larger prior to continental collision. Hence, a direct relationship between the adakitic melts and the subduction along the Bitlis–Zagros suture can be ruled out. All these arguments clearly suggest that the Paleocene to Early Eocene adakitic rocks in the Pontides and in the northernmost part of the Anatolide–Tauride block are not related to an active subduction.

Slab-breakoff after the collision along the İzmir–Ankara–Erzincan suture is proposed as a cause of Eocene magmatism (e.g. Altunkaynak, 2007; Boztuğ et al., 2007; Dilek et al., 2010; Keskin et al., 2008). In case of a slab-breakoff, Eocene magmatism should be confined to the Eastern Pontides. However, the Eocene magmatism occurs on both sides of the İzmir–Ankara suture. We therefore regard the slab breakoff as an unlikely cause for Eocene magmatism.

During the Paleocene to Early Eocene, formation of multiple north-vergent thrust slices led to a significant crustal shortening, and thus to crustal thickening in the Eastern Pontides (Fig. 1b; Okay and Şahintürk, 1997; Okay et al., 1997). This was followed by a regional marine transgression during the Middle Eocene (Lutetian) both in the Pontides and in the Anatolide–Tauride block due to regional extension probably associated with orogenic collapse. Thickened crust is gravitationally not in equilibrium, and tends to spread laterally attented by the formation of large extensional faults (e.g. Dewey, 1988; Rey et al., 2001). It is generally inferred that extentional collapse occurs especially where (i) lower part of the conductive thermal boundary layer is convectively removed (e.g. Houseman et al., 1981) or (ii) the lowermost lithosphere detaches from the crust and founders into less dense astenospheric mantle (lithospheric delamination; e.g. Bird, 1979; Kay and Kay, 1993). The removed lithospheric root is replaced by lower-density astenospheric mantle in both models. Both models predict rapid regional uplift before crustal extension and abrupt change in thermal state leading to voluminous magmatism whereby the astenosphere is also involved in partial melting due to decompression. In the case of the Eastern Pontides, the available geochemical data display a pronounced subduction-influenced signature, and unambiguously asthenosphere-derived magmatism is so far unknown.

On the basis of the Sr–Nd isotopic and incompatible trace element similarities between the Early Eocene and Middle Eocene rocks, we propose the following picture for the genesis of the Early Eocene adakitic and Middle Eocene granitic rocks: due to the buoyancy, a basaltic melt originating from the lithospheric mantle would not pond until it reaches the Moho (e.g. Fyfe, 1992; Herzberg et al., 1983). The ponding magma can only crystallize garnet, or remelt formerly underplated magmas, leaving garnet and hornblende in the residuum, only if the Moho is located at depths ≥43 km. This was probably the case during the

Paleocene to Early Eocene time. During the Middle Eocene, the crust was thinned and the Moho was located at shallower depths, leading to disappearance of garnet as a fractionating or residual phase.

11. Conclusions

Early Eocene adakitic quartz diorites, leucogranodiorites and dacitic porphyritic dikes in the Ağvanis Massif (Eastern Pontides) were generated in a late- to post-collisional compressive tectonic setting, when the crust was undergoing high exhumation and uplift rates. Adakitic signature is common in the Paleocene to Early Eocene rocks of quartz dioritic to granitic compositions throughout the Pontides and the northernmost part of the Anatolide–Tauride block. Partial melting of the lowermost parts of the thickened crust in concert with crystal fractionation is the most plausible mechanism for the generation of the adakitic signature. By the Middle Eocene, the regional tectonic regime changed from contraction to extension, leading to marine transgression associated with voluminous calc-alkaline basaltic to dacitic magmatism. The extensional tectonics gave rise to thinning of the thickened crust, thus to the disappearance of the adakitic signature.

Acknowledgements

This study was supported by the TÜBİTAK grant #109Y059 as well as by the KTÜ BAB, TÜBA and TÜBA-GEBIP programs. We gratefully acknowledge the careful reviews by Pat Castillo and an anonymous referee. Special thanks are due to İskender Kurt and İsmail Yücel for logistic help during field work, Murat Kayıkçı for cutting rock slices, to Ilona Fin and Oliver Wienand for preparing numerous thin sections, to Alexander Varychev and Hans-Peter Meyer for their assistance during SEM and EPMA work and to Gürsel Sunal and Sabah Yılmaz-Şahin for sharing their unpublished data with us.

References

Adamia, Sh.A., Lordkipanidze, M.B., Zakariadze, G.S., 1977. Evolution of an active continental margin as exemplified by the Alpine history of the Caucasus. Tectonophysics 40, 183–199.

Akın, H., 1979. Geologie, Magmatismus und Lagerstättenbildung im ostpontischen Gebirge/Türkei aus der Sicht der Plattentektonik. Geologische Rundschau 68, 253–283.

Alonso-Perez, R., Müntener, O., Ulmer, P., 2009. Igneous garnet and amphibole fractionation in the roots of island arcs: experimental constraints on H_2O undersaturated andesitic liquids. Contributions to Mineralogy and Petrology 157, 541–558.

Altherr, R., Topuz, G., Siebel, W., Şen, C., Meyer, H.-P., Satır, M., Lahaye, Y., 2008. Geochemical and Sr–Nd–Pb isotopic characteristics of Paleocene plagioleucitites from the Eastern Pontides (NE Turkey). Lithos 105, 149–161.

Altınkaynak, L., 2001. Ağvanis Masifi doğu kesimi ve çevre kayaçlarının jeolojisi, jeokimyası, petrojenezi ve kökeni. Yayınlanmamış doktora tezi, Karadeniz Teknik Üniversitesi, Trabzon, 279 pp.

Altunkaynak, S., 2007. Collision-driven slab breakoff magmatism in northwestern Anatolia, Turkey. Journal of Geology 115, 63–82.

Anderson, J.L., Smith, D.R., 1995. The effect of temperature and oxygen fugacity on Al-in-hornblende barometry. American Mineralogist 80, 549–559.

Arslan, M., Aslan, Z., 2006. Mineralogy, petrography and whole-rock geochemistry of the Tertiary granitic intrusions in the Eastern Pontides, Turkey. Journal of Asian Earth Sciences 27, 177–193.

Aslan, Z., 2010. U–Pb zircon SHRIMP age, geochemical and petrographical characteristics of tuffs within calc-alkaline Eocene volcanics around Gümüşhane (NE Turkey), Eastern Pontides. Neues Jahrbuch für Mineralogie Abhandlungen 187, 329–346.

Atherton, M.P., Petford, N., 1993. Generation of sodium-rich magmas from newly underplated basaltic crust. Nature 362, 144–146.

Bazhenov, M.L., Burtman, V.S., 2002. Eocene palaeomagnetism of the Caucasus (southwest Georgia): oroclinal bending in the Arabian syntaxis. Tectonophysics 344, 247–259.

Bindeman, I.N., Eiler, J.M., Yogodzinski, G.M., Tatsumi, Y., Sterne, C.R., Grove, T.L., Portnyagin, M., Hoernle, K., Danyushevsky, L.V., 2005. Oxygen isotope evidence for slab melting in modern and ancient subduction zones. Earth and Planetary Science Letters 235, 480–496.

Bird, P., 1979. Continental delamination and the Colorado Plateau. Journal of Geophysical Research 84, 7561–7571.

Bohlen, S.R., Montana, A., Kerrick, D.M., 1991. Precise determinations of the equilibria kyanite = sillimanite and kyanite = andalusite and a revised triple point for Al_2SiO_5 polymorphs. American Mineralogist 76, 677–680.

Boynton, W.V., 1984. Cosmochemistry of the rare earth elements: meteorite studies. In: Henderson, P. (Ed.), Rare Earth Element Geochemistry. Elsevier, Amsterdam, pp. 63–114.

Boztuğ, D., 2008. Petrogenesis of the Kösedağ Pluton, Suşehri-NE Sivas, East-Central Pontides, Turkey. Turkish Journal of Earth Sciences 17, 241–262.

Boztuğ, D., Jonckheere, R., Wagner, G.A., Yeğingil, Z., 2004. Slow Senonian and fast Palaeocene–Early Eocene uplift of the granitoids in the Central Eastern Pontides, Turkey: apatite fission-track results. Tectonophysics 382, 213–228.

Boztuğ, D., Erçin, A.I., Kuruçelik, M.K., Göç, D., Kömür, I., Iskenderoğlu, A., 2006. Geochemical characteristics of the composite Kaçkar batholith generated in a Neo-Tethyan convergence system, Eastern Pontides, Turkey. Asian Journal of Earth Sciences 27, 286–302.

Boztuğ, D., Jonckheere, R., Wagner, G.A., Erçin, A.I., Yegingil, Z., 2007. Titanite and zircon fission-track dating resolves successive igneous episodes in the formation of the composite Kackar batholith in the Turkish Eastern Pontides. International Journal of Earth Sciences 96, 875–886.

Castillo, P.R., 2008. Origin of the adakite–high-Nb basalt association and its implications for postsubduction magmatism in Baja California, Mexico. Geological Society of America Bulletin 120, 451–462.

Cherniak, D.J., Watson, E.B., 2000. Pb diffusion in zircon. Chemical Geology 172, 5–24.

Chiaradia, M., Müntener, O., Beate, B., Fontignie, D., 2009. Adakite-like volcanism of Ecuador: lower crust magmatic evolution and recycling. Contributions to Mineralogy and Petrology 158, 563–588.

Dahl, P.S., 1996. The effects of composition on retentivity of argon and oxygen in hornblende and related amphiboles: a field-tested empirical model. Geochimica et Cosmochimica Acta 60, 3687–3700.

Defant, M.J., Drummond, M.S., 1990. Derivation of some modern arc magmas by partial melting of young subducted lithosphere. Nature 347, 662–665.

Dewey, J.F., 1988. Extensional collapse of orogens. Tectonics 7, 1123–1139.

Dilek, Y., Imamverdiyev, N., Altunkaynak, Ş., 2010. Geochemistry and tectonics of Cenozoic tectonics in the Lesser Caucasus (Azerbaijan) and its peri-Arabian region: collision-induced mantle dynamics and its magmatic fingerprint. International Geology Review 52, 536–578.

Elmas, A., Yılmaz, Y., 2003. Development of an oblique subduction zone-tectonic evolution of the Tethys suture zone in southeast Turkey. International Geology Review 45, 827–840.

Eyüboğlu, Y., Santosh, M., Chung, S.-L., 2011a. Crystal fractionation of adakitic magmas in the crust-mantle transition zone: petrology, geochemistry and U–Pb zircon chronology of the Seme adakites, Eastern Pontides, NE Turkey. Lithos 121, 151–166.

Eyüboğlu, Y., Chung, S.-L., Santosh, M., Dudas, F.O., Akaryalı, E., 2011b. Transition from shoshonitic to adakitic magmatism in the Eastern Pontides. NE Turkey: implications for slab window melting. Gondwana Research 19, 412–429.

Fyfe, W.S., 1992. Magma underplating of the continental crust. Journal of Volcanology and Geothermal Research 50, 33–40.

Gradstein, F., Ogg, J., Smith, A., 2004. A Geologic Time Scale. 589 pp. Cambridge University Press, Cambridge, U.K.

Grove, M., Harrison, T.M., 1996. ^{40}Ar diffusion in Fe-rich biotite. American Mineralogist 81, 940–951.

Gürbüz, K., Gül, M., 2005. Evolution of and factors controlling Eocene sedimentation in the Darende-Balaban basin, Malatya (Eastern Turkey). Turkish Journal of Earth Sciences 14, 311–335.

Harris, N.B.W., Kelley, S., Okay, A.I., 1994. Postcollision magmatism and tectonics in Northwest Anatolia. Contributions to Mineralogy and Petrology 117, 241–252.

Harrison, T.M., Duncan, I., McDougall, I., 1985. Diffusion of ^{40}Ar in biotite: temperature, pressure and compositional effects. Geochimica et Cosmochimica Acta 49, 2461–2468.

Herzberg, C.T., Fyfe, W.S., Carr, J.J., 1983. Density constraints on the formation of the continental Moho and crust. Contributions to Mineralogy and Petrology 84, 1–5.

Hoisch, T.D., 1990. Empirical calibration of 6 geobarometers for the mineral assemblage quartz + muscovite + biotite + plagioclase + garnet. Contributions to Mineralogy and Petrology 104, 225–234.

Hoisch, T.D., 1991. Equilibria within the mineral assemblage quartz + muscovite + biotite + garnet + plagioclase, and implications for the mixing properties of octahedrally coordinated cations in muscovite and biotite. Contributions to Mineralogy and Petrology 108, 43–54.

Holdaway, M.J., Mukhopadhyay, B., 1993. A reevaluation of the stability of andalusite: thermochemical data and phase diagram for the aluminium silicates. American Mineralogist 78, 298–315.

Houseman, G.A., McKenzie, D.P., Molnar, P., 1981. Convective instability of a thickened boundary layer and its relevance for the thermal evolution of the continental convergent belts. Journal of Geophysical Research 86, 6115–6132.

Jacobsen, S.B., Wasserburg, G.J., 1980. Sm–Nd isotopic evolution of chondrites. Earth and Planetary Science Letters 50, 139–155.

Kadıoğlu, Y.K., Dilek, Y., 2010. Structure and geochemistry of the adakitic Horoz granitoid, Bolkar Mountains, south-central Turkey, and its tectonomagmatic evolution. International Geology Review 52, 505–535.

Karacık, Z., Yılmaz, Y., Pearce, J.A., Ece, O.I., 2008. Petrochemistry of the south Marmara granitoids, northwest Anatolia, Turkey. International Journal of Earth Sciences 97, 1181–1200.

Karaoğlan, F., Parlak, O., Klötzli, U., Thöni, M., Koller, F., 2009. Geochronology and isotope geochemistry of the ophiolites and granitoids along the southeast Anatolian orogonic belt. Mitteilungen der Österreichischen Geologischen Gesellschaft 155.

Karslı, O., Chen, B., Aydın, F., Şen, C., 2007. Geochemical and Sr–Nd–Pb isotopic compositions of the Eocene Dölek and Sarıçiçek Plutons, Eastern Turkey: ımplications for magma interaction in the genesis of high-K calc-alkaline granitoids in a post-collision extensional setting. Lithos 98, 67–96.
Karslı, O., Dokuz, A., Uysal, I., Aydın, F., Kandemir, R., Wijbrans, J., 2010. Generation of the Early Cenozoic adakitic volcanism by partial melting of mafic lower crust, Eastern Turkey: ımplications for crustal thickening to delamination. Lithos 114, 109–120.
Kay, R.W., Kay, S.M., 1993. Delamination and delamination magmatism. Tectonophysics 219, 177–189.
Kaygusuz, A., Arslan, M., Siebel, W., Şen, C., 2011. Geochemical and Sr–Nd isotopic characteristics of post-collisional calc-alkaline volcanics in the Eastern Pontides (NE Turkey). Turkish Journal of Earth Sciences 20, 137–159.
Keskin, M., Genç, S.C., Tüysüz, O., 2008. Petrology and geochemistry of post-collisional Middle Eocene volcanic units in north-central Turkey: evidence for magma generation by slab breakoff following the closure of the Northern Neotethys Ocean. Lithos 104, 267–305.
Kibici, Y., Ilbeyli, N., Yıldız, A., Bağcı, M., 2008. Geochemical constraints on the genesis of the Günyüzü pluton, northwest Anatolia, Turkey. International Geology Review 50, 931–947.
Kürkçüoğlu, B., Furman, T., Hanan, B., 2008. Geochemistry of post-collisional mafic lavas from the North Anatolian Fault zone, northwestern Turkey. Lithos 101, 416–436.
Kuşçu, I., Kuscu, G.G., Tosdal, R.M., Ulrich, T.D., Friedman, R., 2010. Magmatism in the southeastern Anatolian orogenic belt: transition from arc to post-collisional setting in an evolving orogen. In: Stephenson, R.A., Kaymakçı, N., Sosson, M., Starostenko, V., Bergerat, F. (Eds.), Sedimentary basin tectonics from the Black Sea and Caucasus to the Arabian Platform: Geological Society, London. Special Publication, 340, pp. 437–460.
Lee, J.K.W., Williams, I.S., Ellis, D.J., 1997. Pb, U and Th diffusion in natural zircon. Nature 390, 159–161.
Liew, T.C., Hofmann, A.W., 1988. Precambrian crustal components, plutonic associations, plate environment of the Hercynian Fold Belt of central Europe: indications from a Nd and Sr isotopic study. Contributions to Mineralogy and Petrology 98, 129–138.
López, S., Castro, A., 2001. Determination of the fluid-absent solidus and supersolidus phase relationships of MORB-derived amphibolites in the range 4–14 kbar. American Mineralogist 86, 1396–1403.
Ludwig, K.R., 2003. Isoplot/Ex 3.00. A Geochronological Toolkit for Microsoft Excel. Berkely Geochronological Center, Special Publication, No. 4.
Macpherson, C.G., Dreher, S.T., Thirlwall, M.F., 2006. Adakites without slab melting: high pressure differentiation of island arc magma, Mindanao, the Philippines. Earth and Planetary Science Letters 243, 581–593.
Martin, H., Smithies, R.H., Rapp, R., Moyen, J.F., Champion, D., 2005. An overview of adakite, tonalite–trondhjemite–granodiorite (TTG), and sanukitoid: relationships and some implications for crustal evolution. Lithos 79, 1–24.
Moyen, J.-F., 2009. High Sr/Y and La/Yb ratios: The meaning of the "adakitic signature". Lithos 112, 556–574.
Müntener, O., Kelemen, P.B., Grove, T.L., 2001. The role of H_2O during crystallization of primitive arc magmas under uppermost mantle conditions and genesis of igneous pyroxenites: an experimental study. Contributions to Mineralogy and Petrology 141, 643–658.
Nebert, K., 1961. Der geologische Bau der Einzugsgebiete Kelkit Çay und Kızılırmak (NE Anatolien). Bulletin. Mineral Research and Exploration Institute (Turkey) 57, 1–51.
Okay, A.I., 1984. The geology of the Ağvanis metamorphic rocks and neighbouring formations. Bulletin. Mineral Research and Exploration Institute (Turkey) 99 (100), 16–36.
Okay, A.I., Şahintürk, Ö., 1997. Geology of the Eastern Pontides. In: Robinson, A.G. (Ed.), Regional and Petroleum Geology of the Black Sea and Surrounding Region: American Association of Petroleum Geologists (AAPG) Memoir, No. 68, pp. 291–311.
Okay, A.I., Tüysüz, O., 1999. Tethyan sutures of northern Turkey. In: Durand, B., Jolivet, L., Horváth, F., Séranne, M. (Eds.), The Mediterranean Basins: Tertiary extension within the Alpine orogen: Geological Society London Special Publication, 156, pp. 475–515.
Okay, A.I., Şahintürk, Ö., Yakar, H., 1997. Stratigraphy and tectonics of the Pulur (Bayburt) region in the Eastern Pontides. Bulletin of the Mineral Research and Exploration Institute 119, 1–24.
Okay, A.I., Zattin, M., Cavazza, W., 2010. Apatite fission-track data for Miocene Arabia–Eurasia collision. Geology 38, 35–38.
Önal, A., Boztuğ, D., Kürüm, S., Harlavan, Y., Arehart, G., Arslan, M., 2005. K–Ar age determination, whole-rock and oxygen isotope geochemistry of the post-collisional Bizmişen and Çaltı plutons, SW Erzincan, eastern Central Anatolia, Turkey. Geological Journal 40, 457–476.
Özgülük, Y., Ustaömer, T., Ustaömer, P.A., Gerdes, A., 2009. Petrology and U/Pb geochronology of Gökseki metatrondhjemite (Ağvanis metamorphic), E Pontides: early Lutetian magmatism and subsequent metamorphism and deformation. 62nd Geological Kurultai of Turkey, Ankara, pp. 500–501.
Özkaya, I., 1991. Evolution of a Tertiary volcanogenic trough in SW Turkey — the Alakaya basins in the Lycian belt. Geologische Rundschau 80, 657–668.
Passchier, C.W., Trouw, R.A.J., 2005. Microtectonics. 366 pp. 2nd edition with CD. Springer Verlag3-540-64003-7.
Pattison, D.R.M., 1992. Stability of andalusite and sillimanite and the Al_2SiO_5 triple point: constraints from the Ballachulish aureole, Scotland. Journal of Geology 100, 423–446.
Peacock, S.M., Rushmer, T., Thompson, A.B., 1994. Partial melting of subducting oceanic-crust. Earth and Planetary Science Letters 121, 227–244.
Peccerillo, A., Taylor, S.R., 1976. Geochemistry of Eocene calc-alkaline volcanic rocks from the Kastamonu area, northern Turkey. Contributions to Mineralogy and Petrology 58, 63–81.
Pelin, S., 1977. Geological study of the area southeast of Alucra (Giresun), with special reference to its petroleum potential (in Turkish) Karadeniz Teknik Üniversitesi, Yayın, No 87, p. 103.
Perinçek, D., 1990. Hakkari ili ve dolayının stratigrafisi, Güneudoğu Anadolu, Türkiye. Türkiye Petrol Jeologları Derneği Bülteni 2, 21–68.
Petford, N., Atherton, M., 1996. Na-rich partial melts from newly underplated basaltic crust: the Cordillera Blanca Batholith, Peru. Journal of Petrology 37, 1491–1521.
Pouchou, J.L., Pichoir, F., 1984. A new model for quantitative analyses. I. Application to the analysis of homogeneous samples. La Recherche Aérospatiale 3, 13–38.
Pouchou, J.L., Pichoir, F., 1985. 'PAP' ($\varphi-\rho-Z$) correction procedure for improved quantitative microanalysis. In: Armstrong, J.T. (Ed.), Microbeam Analysis. San Francisco Press, San Francisco, CA, pp. 104–106.
Pourteau, A., Candan, O., Oberhänsli, R., 2010. High-pressure metasediments in central Turkey: constraints on the Neotethyan closure history. Tectonics 29 TC5004.
Prouteau, G., Scaillet, B., 2003. Experimental constraints on the origin of the 1991 Pinatubo dacite. Journal of Petrology 44, 2203–2241.
Ramezani, J., Tucker, R.D., 2003. The Saghand region, central Iran: U–Pb geochronology, petrogenesis and implications for Gondwana tectonics. American Journal of Science 303, 622–665.
Rapp, R.P., 1995. Amphibole-out phase boundary in partially melted metabasalt, its control over liquid fraction and composition, and source permeability. Journal of Geophysical Research 100, 15601–15610.
Rapp, R.P., Watson, E.B., 1995. Dehydration melting of metabasalt at 8–32 kbar: implications for continental growth and crust-mantle recycling. Journal of Petrology 36, 891–931.
Rapp, R.P., Watson, E.B., Miller, C.F., 1991. Partial melting of amphibolite/eclogite and the origin of Archean trondhjemites and tonalites. Precambrian Research 51, 1–25.
Rey, P., Vanderhaeghe, O., Teyssier, C., 2001. Gravitational collapse of the continental crust: definition, regimes and modes. Tectonophysics 342, 435–449.
Rice, S.P., Robertson, A.H.F., Ustaömer, T., İnan, N., Taslı, K., 2009. Late Cretaceous-Early Eocene tectonic development of the Tethyan suture zone in the Erzincan area, Eastern Pontides, Turkey. Geological Magazine 146, 567–590.
Robertson, A.H.F., Ustaömer, T., Parlak, O., Ünlügenç, Ü.C., Taslı, K., İnan, N., 2006. The Berit transect of the Tauride thrust belt, S Turkey: late Cretaceous-early Cenozoic accretionary/collisional processes related to closure of the Southern Neotethys. Journal of Asian Earth Sciences 27, 108–145.
Robertson, A.H.F., Parlak, O., Rızaoğlu, T., Ünlügenç, Ü.C., İnan, N., Tasli, K., Ustaömer, T., 2007. Tectonic evolution of the South Tethyan ocean: evidence from the Eastern Taurus Mountains (Elaziğ region, SE Turkey). Geological Society London Special Publications 272, 231–270.
Schmidt, M.W., Poli, S., 2004. Magmatic epidote. In: Liebscher, A., Franz, G. (Eds.), Epidotes. : Reviews in Mineralogy and Geochemistry, 56. Mineralogical Society of America and Geochemical Society, Washington DC, pp. 399–430.
Schwarz, W.H., Trieloff, M., 2007. Intercalibration of $^{40}Ar/^{39}Ar$ age standards NL-25, HB3gr hornblende, GA1550, SB-3, HD-B1 biotite and BMus/2 muscovite. Chemical Geology 242, 218–231.
Şen, C., Dunn, T., 1994. Dehydration melting of a basaltic composition amphibolite at 1.5 and 2.0 GPa: implications for the origin of adakites. Contributions to Mineralogy and Petrology 117, 394–409.
Şengör, A.M.C., Yılmaz, Y., 1981. Tethyan evolution of Turkey: a plate tectonic approach. Tectonophysics 75, 181–241.
Staudigel, H., Davies, G.R., Hart, S.R., Marchant, K.M., Smith, B.M., 1995. Large scale isotopic Sr, Nd and oxygen isotopic anatomy of altered oceanic crust: DSDP/ODP sites 417/418. Earth and Planetary Science Letters 130, 169–185.
Steiger, R.H., Jäger, E., 1977. Subcommission on geochronology: convention on the use of decay constants in geo- and cosmochronlogy. Earth and Planetary Science Letters 36, 359–362.
Stöcklin, J., 1971. Stratigraphic Lexicon of Iran. Part 1: Central, North and East Iran. Geological Survey of Iran, Tehran. 338 pp.
Sun, S.-S., McDonough, W.F., 1989. Chemical and isotopic systematics of oceanic basalts: implications for mantle composition and processes. In: Saunders, A.D., Norry, M.J. (Eds.), Magmatism in the Ocean Basins: Geological Society London Special Publication, 42, pp. 313–345.
Temizel, İ., Arslan, M., 2009. Mineral chemistry and petrochemistry of post-collisional Tertiary mafic to felsic cogenetic volcanics in the Ulubey (Ordu) area, Eastern Pontides, NE Turkey. Turkish Journal of Earth Sciences 18, 29–53.
Tokel, S., 1977. Dogu Karadeniz Bölgesinde Eoson yaşlı kalkalkalen andezitler ve jeotektonizma. Türkiye Jeoloji Kurumu Bülteni 20, 49–54.
Topuz, G., Altherr, R., Satir, M., Schwarz, W.H., 2004. Low-grade metamorphic rocks from the Pulur complex, NE Turkey: implications for the pre-Liassic evolution of the Eastern Pontides. International Journal of Earth Sciences 93, 72–91.
Topuz, G., Altherr, R., Schwarz, W.H., Siebel, W., Satır, M., Dokuz, A., 2005. Post-collisional plutonism with adakite-like signatures: the Eocene Saraycık granodiorite (Eastern Pontides, Turkey). Contributions to Mineralogy and Petrology 150, 441–455.
Topuz, G., Altherr, R., Siebel, W., Schwarz, W.H., Zack, T., Hasözbek, A., Barth, M., Satır, M., Şen, C., 2010. Carboniferous high-potassium I-type granitoid magmatism in the Eastern Pontides: the Gümüşhane pluton (NE Turkey). Lithos 116, 92–110.
Türkmen, I., İnce, N., Aksoy, E., Kaya, M., 2001. Elazığ yöresinin Eosen stratigrafisi ve paleocoğrafyası ile ilgili yeni bulgular. Yerbilimleri 24, 81–95.
Ustaömer, P.A., Ustaömer, T., Collins, A.S., Reischpeitsch, J., 2009. Lutetian arc-type magmatism along the southern Eurasian margin: new U–Pb LA-ICPMS and whole-rock geochemical data from Marmara Island, NW Turkey. Mineralogy and Petrology 96, 177–196.

Vincent, S.J., Allen, M.B., Ismail-Zadeh, A.D., Flecker, R., Foland, K.A., Simmons, M.D., 2005. Insights from the Talysh of Azerbaijan into the Paleogene evolution of the South Caspian region. Geological Society of America Bulletin 117, 1513–1533.

Wang, Q., Wyman, D.A., Xu, J.-F., Zhao, Z.-H., Jian, P., Xiong, X.-L., Bao, Z.-W., Li, C.-F., Bai, Z.-H., 2006. Petrogenesis of Cretaceous adakitic and shoshonitic igneous rocks in the Luzong area, Anhui Province (eastern China): ımplications for geodynamics and Cu–Au mineralization. Lithos 89, 424–446.

Winther, K.T., 1996. An experimentally based model for the origin of tonalitic and trondhjemitic melts. Chemical Geology 127, 43–59.

Winther, K.T., Newton, R.C., 1991. Dehydration-melting of solid amphibolite at 10 kbar: textural development, liquid interconnectivity and applications to the segregation of magmas. Mineralogy and Petrology 44, 151–179.

Yaxley, G.M., Green, D.H., 1998. Reactions between eclogite and peridotite; mantle refertilisation by subduction of oceanic crust. Swiss Bulletin of Mineralogy and Petrology 78, 243–255.

Yiğitbaş, E., Yılmaz, Y., 1996. New evidence and solution to the Maden complex controversy of the Southeast Anatolian orogenic belt (Turkey). Geologische Rundschau 85, 250–263.

Yılmaz, A., Adamia, S., Chabukiani, A., Chkhotua, T., Erdogan, K., Tuzcu, S., Karabiyikoglu, M.F., 2000. Structural correlation of the southern Transcaucasus (Georgia)–Eastern Pontides (Turkey). In: Bozkurt, E., Winchester, J.A., Piper, J.D.A. (Eds.), Tectonics and Magmatism in Turkey and the Surrounding Area: Geological Society London Special Publication, 173, pp. 171–182.